# Analysis of a Parsimonious Coupled Model of the Equatorial Pacific Surface Temperature Change

**Simon D.A. Thomas**

**Supervisor:**

**Dr. Daniel C. Jones**

**British Antarctic Survey**

**August 4, 2021**

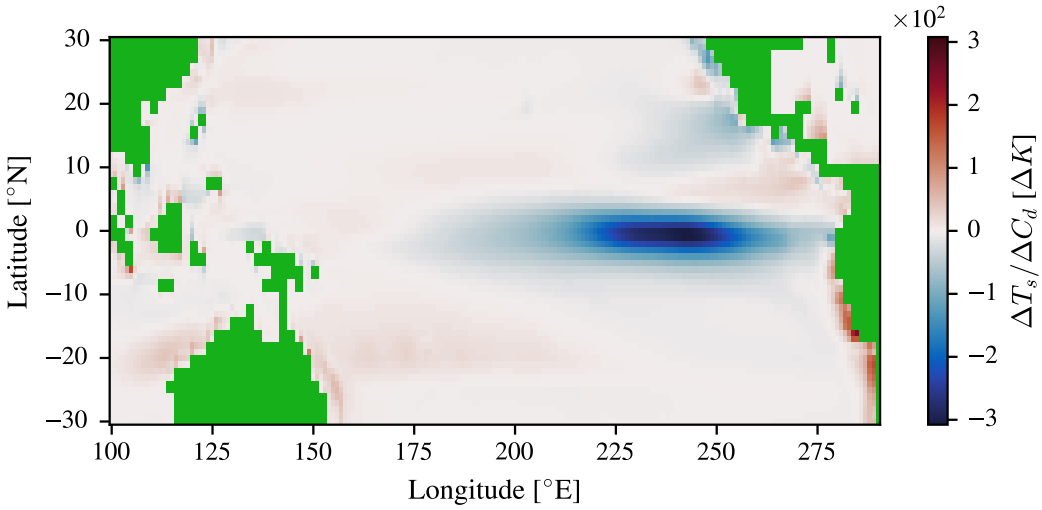


A report submitted for the partial fulfilment of
the degree requirements of Master of Research
in Environmental Data Science.

4990/5000 words

UNIVERSITY OF
CAMBRIDGE

# Contents



**Declaration:** This report is the result of my own work and includes nothing which is the outcome of work done in collaboration, except where specifically indicated in the text or bibliography.

**Documentation:** https://seager19.readthedocs.io

**Github:** https://github.com/sdat2/seager19. The scripts automatically download all necessary data from Dropbox.

**Model run results (weights and biases):** https://wandb.ai/sdat2/seager19. Each model run includes an exact specification of the input parameters, code version, and python / gfortran environment.

**Docker image:** https://hub.docker.com/repository/docker/sdat2/seager19

# Analysis of a Parsimonious Coupled Model of the Equatorial Pacific Surface Temperature Change

Simon Thomas, sdat2@cam.ac.uk

August 4, 2021

**Abstract**

This report reassembles a parsimonious coupled model that was created to explain the bias in the trend of the El Niño southern oscillation in models. When forced with ECMWF reanalysis fields, it can reproduce the trend observed in the ORAS4 reanalysis product that was forced with the same fields. It shows that the CMIP5 bias in the trend in NINO3.4 from 1958-2017 could be due to a product of the CMIP5 bias in relative humidity and sea surface winds, which is shown through exchanging ECMWF mean fields for CMIP5 multimodel mean fields. The replacements of mean relative humidity, mean wind speed, and both together, lead to increases in the NINO3.4 trend of 0.31±0.03 K, 0.054±0.005 K, and 0.47±0.04 K respectively when tested with a range of plausible inputs. This is congruent with the observed difference of 0.478 K between the ECMWF/ORAS4 reanalysis product and the CMIP5 multimodel mean.

I investigate how reliable the results from this model might be by varying the free parameters and find that, as far as tested, the model is not overly sensitive to subjective inputs. It is therefore plausible that observed bias in the increase in sea surface temperature is caused by excess humidity, and insufficient wind speed over the cold tongue – are reinforced as credible, as the model is not overly sensitive to variation of the free parameters. This project relies on physical modelling rather than more advanced statistical techniques.

## 1 Introduction

Global warming could lead to a stronger temperature gradient across the equatorial Pacific which would move the balance towards La Niña (stronger gradient) and away from El Niño (weaker gradient) [1]. This expectation matches observations. However, Cane et al. 1997 [1], highlighted that the state-of-the-art climate models failed to reproduce this pattern. This bias has been found in every subsequent generation of climate models including CMIP5 in Seager et al. 2019 ([2], henceforth S19) (see Figure 1).

This bias is normally mentioned alongside the double intertropical convergence zone (ITCZ) bias, where climate models fail to produce the observed asymmetry in precipitation over the tropical Pacific [3] and this joint bias is known as the "Pacific double ITCZ cold tongue bias". While bias correction algorithms may be able to alleviate these problems it is likely that it still has a negative effect on the accuracy of future risk predictions, and any planned mitigation [2, 4].

This bias will have a substantial effect on the environmental risks that such climate models might predict; North Atlantic tropical cyclone (TC) activity appears to be suppressed during El Niño years, and enhanced during La Niña years [5, 6]. Therefore this bias could lead to an under-prediction in the number of TCs on the United States East Coast and their accompanying risks (e.g. storm surges). The sign of the El Niño Southern Oscillation also effects the climate of many regions of the globe, changing the risks of floods, droughts and extreme heat through its teleconnections [7].

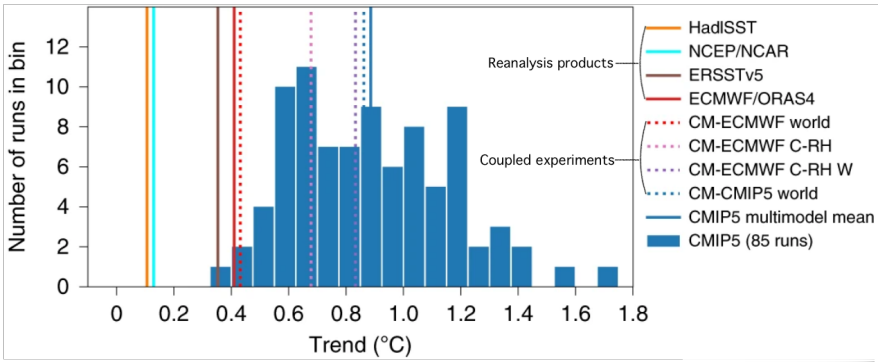


Figure 1: Figure 5(e) from S19. The the 60 year trend up to 2017 in the nino3.4 ocean region (see Figure 2). A comparison between the CMIP5 ensemble members (blue bars), and from the Hadley centre reanalysis (orange), NCEP/NCAR reanalysis (cyan). The red dotted line CM-ECMWF is the coupled model run with ECMWF inputs, which almost reproduces the output of ORAS4, with a trend of approximately 0.41°C. CM-CMIP5 world (purple stripes, the coupled model forced with CMIP5 mean inputs) on the other hand reproduces the CMIP5 mean trend of roughly 0.9°C. S19 shows that this effect can be shown to be a consequence of the relative humidity in CMIP5 being too high over the cold tongue, and the westward winds being too weak, through the difference between CM-ECMWF world and CM-CMIP5 world, where the inputs of humidity and wind speed are changed from ECMWF to the CMIP5 multimodel mean.

S19 showed both that this cold tongue bias exists in CMIP5. They then showed they could use a simple physical coupled model, whose assumptions are appropriate in the tropical Pacific, to reproduce the trend in the historical period when forced with the ECMWF reanalysis product. They then showed that they reproduce CMIP5 bias when forced with CMIP5 humidity and surface wind fields instead (Figure 1). This suggests that the bias is created by insufficient zonal winds over the cold tongue and overly high humidity. The project initially focuses on reassembling the results of the physical model from S19 and reproducing this mechanism in Section 4. One problem with using an idealised model is that the parameters that are used within it may not have measurable physical equivalents, and so for its results to be believable they should hold through a range of plausible parameter values. I first introduce the broad research area in Section 2. After reassembling the coupled model (Section 3), I vary the parameters in the model to show how the trends can be changed (Section 5) in the coupled model to investigate this sensitivity, and I discuss how this work can be built upon (Section 6).

| Ab | Expansion |
|---|---|
| ML | Machine learning |
| GP | Gaussian process |
| CMIP | Coupled model intercomparison project |
| ENSO | El Niño Southern Oscillation |
| S19 | Seager et al. 2019 [2] |
| M86 | Cane and Zebiak 1986 [8] |
| M97 | Cane et al. 1997 [1] |
| SST | Sea surface temperature (°C or K) |

Table 1: Abbreviations (Ab) used in this report.

| Sym | Description |
|---|---|
| $\rho_a$ | Density of air. |
| $\rho_w$ | Density of water. |
| $t$ | Time. |
| $\mathbf{u}$ | Velocity. |
| $p$ | Pressure. |
| $P_r$ | Precipitation |
| $\vec{\tau}$ | Sea surface stress. |
| $\phi$ | Gravitational potential. |
| $T_d$ | Deep water temperature. |
| $T_s$ | Surface temperature. |
| $c_p$ | Heat capacity. |

Table 2: Symbols (Sym) for fluid mechanical equations.

## 2 The Tropical Pacific and El Niño Southern Oscillation

For the equatorial Pacific, the large scale Walker circulation normally consists of the ascent of air over the warm water in the West Pacific, and the descent of air over the East Pacific and South America, so that over there is a persistent westward wind over the equatorial Pacific/ This westward wind causes warm surface water to be transported westward, and cold deep water to upwell along the Peruvian coast, and along the equator at the cold tongue. This corresponds to a shallower thermocline on the East than in the West. This sustains the warmer temperatures in the West Pacific, and colder temperatures in the East Pacific, and so this pattern is self-sustaining.

If the circulation is strengthened, the water in the West Pacific can warm further and can cause stronger upwelling of deep water with a shallower thermocline in the East Pacific. This sustains a stronger Walker circulation which is known as La Niña (positive Bjerknes feedback [7]). If the circulation weakens, it can cause upwelling to be reduced in the East Pacific, and the area of upwelling air to move towards the centre of the Pacific. This is known as El Niño (negative Bjerknes feedback [7]).

To look at an example of what the anomaly in sea surface temperature looks like for each of the canonical surface boxes from the NOAA reanalysis product see Figure 2 (overleaf). In this work, we focus on using the nino3.4 box used by S19, which focuses on the central East Equatorial Pacific, which covers the cold tongue. The reanalysis product shows the presence of particularly strong El Niño events in 1982, 1987 and 1997, which are visible as a positive anomaly in all of the indices. The trend in nino3.4 of $0.38 \pm 0.11$ over the period agrees with that of ECMWF/ORAS4 (Figures 1).

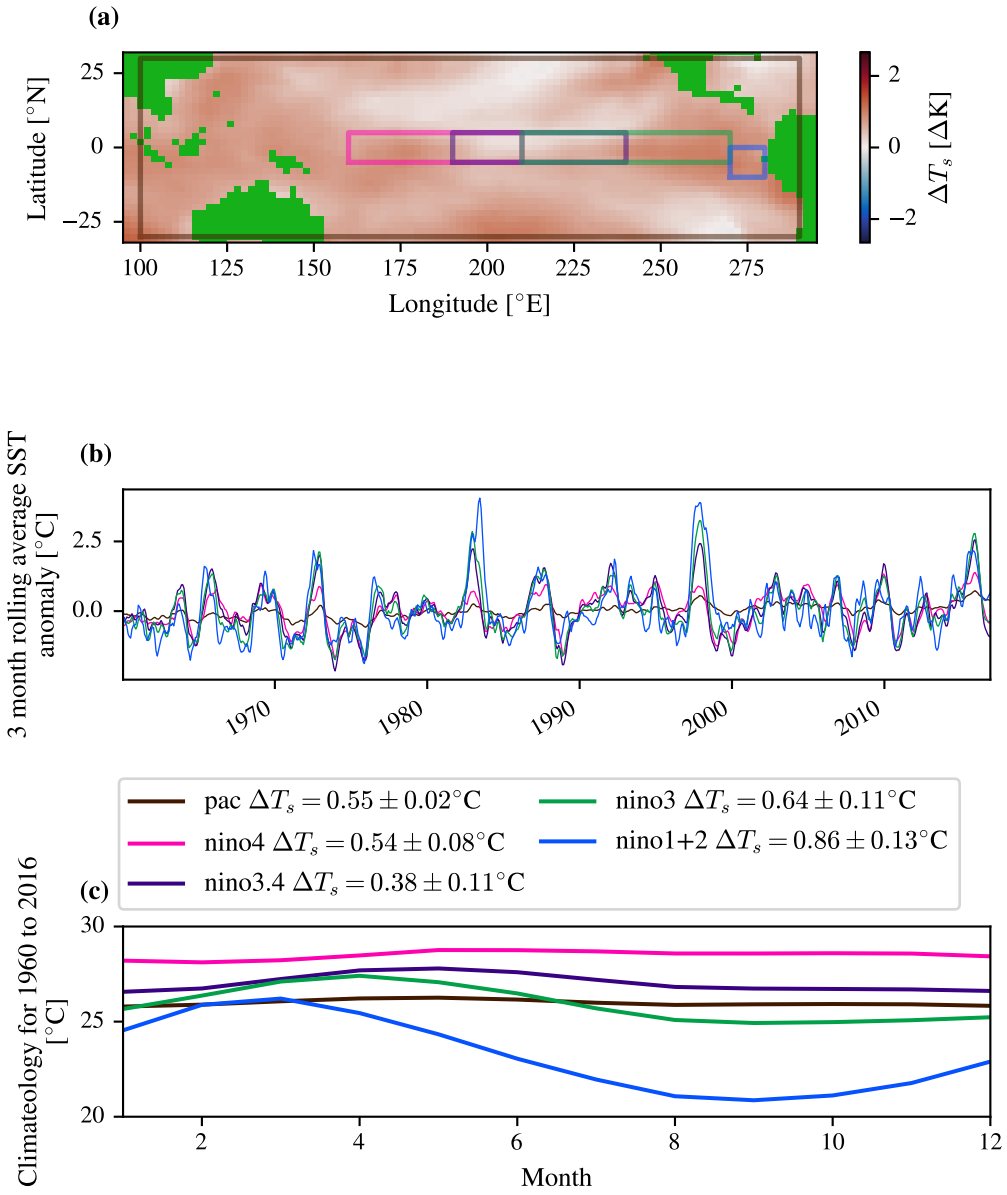


Figure 2: An example of calculating future metrics from a reanalysis of the historical period by NOAA (ERSSTv3.4). (a) Nino index region from index region from UCAR.edu overlaid in the rise calculated from the linear trend at each grid point over 50 years; (b) Niño metrics; (c) climatology of each of the regions over the full time period for the 12 months of the year. Panel (b) shows positive (El Niño) and negative (La Niña) events in the nino3.4 metric, that must have been triggered by the wind stress in the climatology.

# 3 Physical model

## 3.1 Common Model Features

*[An index after a semicolon denotes a partial derivative with respect to that variable.]*

The troposphere and upper ocean layer are both modelled by some number of baroclinic modes following the shallow water equations with linear dynamics in that layer. Both models make the beta plane approximation, where the Coriolis force is approximated to be $f = 2\Omega\lambda = \beta y$, where $\Omega$ is the angular frequency of the rotation of the earth in radians per second and $\lambda$ is the latitude of the point in radians. $\beta$ is the rate of change of Coriolis force with distance, and $y$ is the latitude in metres north and south of the equator. This is equivalent to taking the traditional approximation, where the component of the Coriolis force in the vertical component is ignored, at the same time as taking the small-angle approximation, $\sin\lambda \approx \lambda$ as we assume $\lambda \ll 1$. This means that these models will only be physically plausible a small number of degrees from the equator. Later plots in this report will tend to show the results (-30, 30)°N, but any trends more than 15 degrees from the equator are likely to be unreliable.

Baroclinic vertical modes, also known as internal modes or vertical modes,[1] are a simplification that can be made to the shallow water equations so that a motion is the sum of $N$ modes,

$$\begin{bmatrix} u(x,y,z,t), \\ v(x,y,z,t), \\ \frac{1}{\rho}P(x,y,z,t) \end{bmatrix} = \sum_{m=0}^{\infty} \begin{bmatrix} u'_m(x,y,t), \\ v'_m(x,y,t), \\ gh'_m(x,y,t) \end{bmatrix} A_m(z), \tag{1}$$

where $A_m(z)$ are the solutions to the equation, where $G_m(z) = A_{m;\,z}(z)$,

$$G_{m;\,zz}(z) + \frac{N^2(z)}{c_m^2} G_m(z) = 0, \tag{2}$$

where $N^2(z) = -\frac{g}{\rho_0}\frac{d\rho}{dz}$ is the buoyancy or stratification frequency, $g$ is the gravitational acceleration at that layer, $\rho$ is the density at that depth $z$, and $c_m$ is the mode speed for that mode number (see Cane 1984 [10]). If the stratification, $N^2$, is constant then this equation will admit sinusoidal solutions for $G_m(z)$. These eigenfunctions, $G_m(z)$ are normalised so that they square integrate to the width of the layer,

$$\int_{z_B}^{z_T} G_m^2(z)dz = z_T - z_B, \tag{3}$$

where $Z_T$ and $Z_B$ are the top and bottom of the fluid at equilibrium. For the tropospheric model $G_m(z)$ is taken to at a maximum at the surface ($z = 0$) and the tropopause ($z = z_T$). The boundary conditions for the ocean taken to be that $G_m(D) = 0$ at the sea bottom, and at the surface $G_m(0) = 0$.

## 3.2 Ocean

The ocean component models a shallow water layer with two baroclinic modes underlain by an static abyssal layer of constant temperature, $T_d$ [8, 11, 12, 13, 14, 15]. This is related to the model used in Cane et al. 1986 ([8], henceforth M86), which was the first dynamical model to predict El Niño. It uses the INC integration scheme, which has the basis of being highly stable [16] to calculate the evolution of the model upon a global 1° grid. The buoyancy frequency is highest around the thermocline, and so $A_m(z)$ reaches a maximum around it, focusing the computational resources on resolving its movement. The ocean equations for the surface layer are adapted from the shallow water equations,

[1] Introduction in p. 406 of Cushman & Roisin 2010 [9]

$$\begin{bmatrix} u_{m;\,t} \\ v_{m;\,t} \end{bmatrix} + f \begin{bmatrix} -v_m \\ u_m \end{bmatrix} = -g \begin{bmatrix} -h_{m;\,x} \\ h_{m;\,y} \end{bmatrix} + \begin{bmatrix} \tau_m^x \\ \tau_m^y \end{bmatrix} - r_m \begin{bmatrix} u_m \\ v_m \end{bmatrix}, \tag{4}$$

$$u_{m;\,x} + v_{m;\,y} = -h_{m;\,t} - r_m \cdot h_m, \tag{5}$$

$$f \begin{bmatrix} -v_E \\ u_E \end{bmatrix} = \frac{1}{\rho H^*} \begin{bmatrix} \tau^x \\ \tau^y \end{bmatrix} + r_E \begin{bmatrix} u_E \\ v_E \end{bmatrix}, \tag{6}$$

where Equations 4 & 5 represents the dimensionless equations of baroclinic modes (divided by the constants $U = c_m, H = c_m^2/g$ and $T = (c_m\beta)^{-1/2}$), where $r_m$ is the Newtonian damping rate for each mode. Equation 6 shows how Ekman force created by the wind stress is turned into velocities, in the top 50 m which corresponds to the mixed layer, $u_E$ and $v_E$ that go on to drive the modes as in [11]. The effective height of the model $H^*$ is calculated using height of the surface layer and the effective height of the first two modes $D_1$ and $D_2$,

$$\frac{1}{H^*} = \frac{1}{H_s} - \frac{1}{D_1} - \frac{1}{D_2}, \tag{7}$$

where $H_s$ is the layer of the thermocline. The upwelling to the base of the mixed layer $w_s$ is given by,

$$w_s = H_s \left(u_{s;\,x} + v_{s;\,y}\right) \tag{8}$$

,

which is equivalent to the divergence of the surface current multiplied by the depth of the surface layer $H_s$. The temperature change of the sea surface is calculated by

$$T_{s;\,t} + \begin{bmatrix} u_s \\ v_s \\ w_s \end{bmatrix} \cdot \begin{bmatrix} T_{s;\,x} \\ T_{s;\,y} \\ T_{s;\,z} \end{bmatrix} + \gamma M(w_s) \frac{T_s - T_d}{H_s} = -\frac{\bar{Q} + Q'}{\rho c_{pw} H_s} \tag{9}$$

where $\gamma$ is the entrainment ratio of deep water upwelled to the surface (0.75), $T_s$ is the temperature of the surface layer and $T_d$ is the temperature of the abyssal layer. Only upwelling effects the surface temperature, and so $M(w_s) = 1$ if $w_s > 0, M(w_s) = 0$ if $w_s \leq 0$. $\bar{Q}$ and $Q'$ are given by the surface flux model.

## 3.3 Atmosphere

### 3.3.1 Matsuno Gill Troposphere Model

The Matsuno-Gill [17, 18] model assumes the atmosphere has a constant buoyancy frequency $N^2$, and we assume that the tropospheric motion can be captured by its first baroclinic mode whose velocity profile is given by,

$$\begin{bmatrix} u \\ v \\ w \end{bmatrix} = \begin{bmatrix} u' \cos\left(\pi z / z_T\right) \\ v' \cos\left(\pi z / z_T\right) \\ w' \sin\left(\pi z / z_T\right) \end{bmatrix}, \tag{10}$$

where $z_T$ is the height of the tropopause.

$$(\theta, Q) = (\theta', Q')\left(\theta_0/\theta_{00}\right) \tag{11}$$

The pressure is given by

$$p = p'\left(\rho_0/\rho_{00}\right)\cos\left(\pi z/z_{\mathrm{T}}\right), \tag{12}$$

making the anelastic approximation,

$$(p/\rho_0)_z = g\theta/\theta_{00} \tag{13}$$

and the hydrostatic approximation,

$$p'/\rho_{00} = (gz_{\mathrm{T}}/\pi\theta_{00})\,\theta. \tag{14}$$

The shallow water equations in steady state for the atmosphere are,

$$f\begin{bmatrix}-v\\ u\end{bmatrix} = -\begin{bmatrix}\phi_{;\,x}\\ \phi_{;\,y}\end{bmatrix} - \begin{bmatrix}\varepsilon_u u\\ \varepsilon_v v\end{bmatrix}, \tag{15}$$

$$u_{;\,x} + v_{;\,y} = -Q_1 - \varepsilon_\phi \phi, \tag{16}$$

where $\epsilon_u$ and $\epsilon_v$ are the Raleigh friction rates,n the gravitational potential is given by

$$\phi = -(gz_{\mathrm{T}}/\pi\theta_{00})\,\theta, \tag{17}$$

and the damping rate in the phi direction is given by

$$\varepsilon_\phi = K\pi^2/\left(N^2 z_{\mathrm{T}}^2\right). \tag{18}$$

Where $K$ corresponds to the Newtonian cooling rate. The winds are driven by the modified heating,

$$Q_1 = \frac{g\pi}{N^2\theta_{00}z_{\mathrm{T}}}\left(K\theta_{\mathrm{s}} + Q_{\mathrm{c}}\right) \tag{19}$$

where $Q_c$ is a consequence of the the precipitation $P_r$

$$Q_{\mathrm{c}} = (\pi L/2c_{\mathrm{pa}}\bar{\rho}z_{\mathrm{T}})\,P_r. \tag{20}$$

Where the precipitation is given by

$$P_r = \rho_{\mathrm{a}}c_{\mathrm{E}}W\left(q_{\mathrm{s}} - q_{\mathrm{a}}\right) - \rho_{\mathrm{a}}H_{\mathrm{q}}\nabla\cdot\vec{u}q_{\mathrm{a}} \tag{21}$$

where $q_a = rq_s\,(T_s)$, and we take r=0.7.

### 3.3.2 Surface Flux model

The surface flux model is after [19], where we allow heat to escape through longwave heat flux and latent heat flux, but ignore the so-called sensible heat flux. The sensible heat flux is the conduction of heat from the ocean to the atmosphere, as it is thought to be a small component of the total. The model uses the parameterisation that the effective temperature of the air near the sea surface $T_a = T_s - \delta T$, where $\delta T = 1\mathrm{K}$. The anomaly latent heat flux from the evaporation of water at the surface is given by

$$\Delta Q_{LH} = \rho_a C_E W L(1-r)\frac{dq_s}{dT_s}_{\bar{T}_s}\Delta T_s. \tag{22}$$

The anomaly longwave heat flux from infrared radiated emitted from the surface is given by

$$\Delta Q_{LW} = \epsilon\sigma\bar{T}_s^4\Delta f_1(1-aC^2) + \frac{dQ_{LW}}{dT_s}|_{\bar{T}_s}\Delta T_s. \tag{23}$$

where $C$ is the average cloud cover, which is multiplied by some constant $a$ that is the assumption as to their kind. The derivative of the long wave insulation is given by

$$\frac{dQ_{LW}}{dT_s}|_{\bar{T}_s} = (1-a\bar{C}^2)\epsilon\sigma\bar{T}_s^3\left[4f_1 - f_2\left(\frac{\bar{q}_a\bar{p}_s}{0.622}\right)^{0.5}\left(\frac{\bar{T}_s}{2\bar{q}_s}\frac{dq_s}{dT}|_{T_s} + 4\right)\right] + 12\epsilon\sigma\bar{T}_s^2\delta T_s. \tag{24}$$

## 3.4 Coupling

As the coupling section of the code was not available online, this section interprets the short description in S19 [12], and so it is possible that the implementation may differ. A schematic of the coupling scheme is shown in Figure 4, with model cycles shown. The troposphere model, and the surface flux model are only run once per cycle, rather than being directly coupled at every time step. The ocean sees the troposphere through the increase in the wind surface stress added to the ECMWF reanalysis product. The atmosphere sees the ocean through the average sea surface temperature, and the change in the sea surface temperature over the 60 year period. Similarly, the surface flux model only sees the mean ocean state, and so is not able to adapt to changing parameters. The effect of this is that the model will be unreliable in its representation of any El Niño / La Niña event, but it may be able to capture the trend over the period.

The wind stress trend from the troposphere is added to the initial ECMWF $\vec{\tau}$ value to get the new value for the wind stress applied to the ocean $\vec{\tau}'$ by the relation

$$\vec{\tau}'(x,y,t) = \vec{\tau} + \frac{t-t_0}{t_f-t_0} \cdot \text{taper}(y) \cdot C_d \cdot \rho_a \cdot \bar{W}(x,y) \cdot \Delta\vec{u}(x,y), \tag{25}$$

where $t_f$ is the final time, $t_0$ is the start time, $W$ is the climatological wind from ECMWF, $\Delta\vec{u}(x,y)$ is the trend in the velocities taken from the troposphere model, and the the taper applied is

$$\text{taper}(y) = \begin{cases} 1.0 & \text{if } 20°\text{N} > y > -20°\text{N} \\ (y-25)/5 & \text{if } 20°\text{N} \leq y \leq 25°\text{N} \\ (y+25)/5 & \text{if } -20°\text{N} \geq y \geq -25°\text{N} \\ 0 & \text{if } 25°\text{N} < y \text{ or } y < -25°\text{N} \end{cases}, \tag{26}$$

which is applied because the assumptions behind the atmospheric model would be grossly inaccurate outside that range (e.g. due to the equatorial beta plane approximation). Figure 4 shows a full schematic for the model. Figure 5 shows the final iteration of the coupling scheme with the fields that are passed between the different components. Figure 6 shows that the model converges within 6 iterations for the trend of the nino3.4 to within less than 1% as the final change for a wide variety of drag coefficient $C_d$. Figure 3 shows that the internal variability of the model is a poor reflection of the expected trends, potentially as the model can only couple every 58 years, although it does replicate the expected trend.

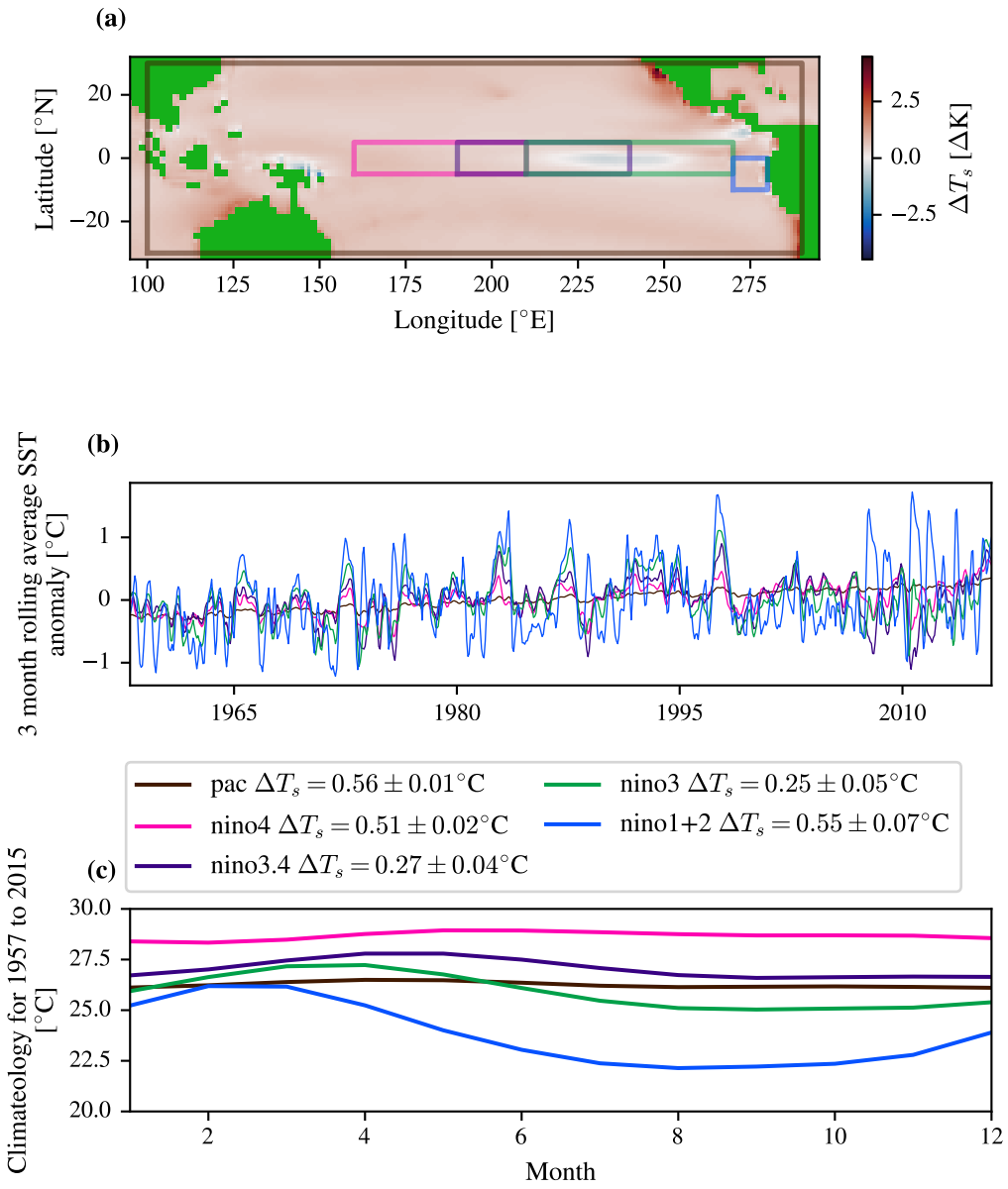


Figure 3: Final coupled model after 6 iterations for the default parameters (a) Niño metrics; (b) climatology of each of the regions over the full time period for the 12 months of the year. Panel (a) shows positive (El Niño) and negative (La Niña) events in the nino3.4 metric, that must have been triggered by the wind stress in the ECMWF reanalysis product, although these are much smaller than those calculated from the ERSSTv5 product (Figure 2).

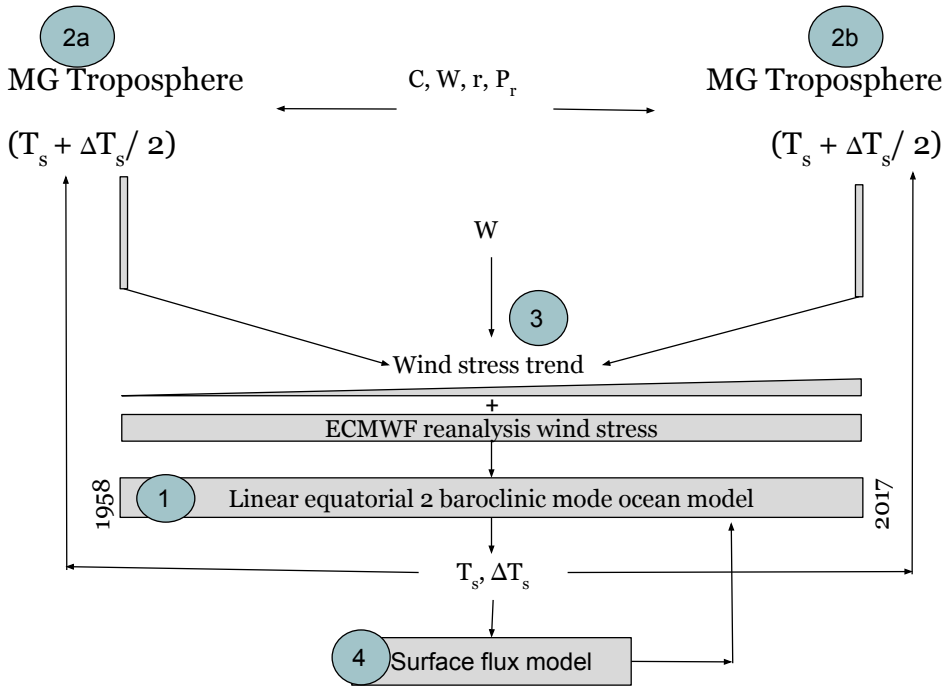


Figure 4: A diagram of the coupled ocean-atmosphere model running between the beginning of 1958 and and the end of 2017. (1) The ocean model is run between 1958 to 2017, and from this, we can calculate the average sea surface temperature of each grid point over the period, and the linear increase in the amount of sea surface temperature (its so-called trend over the period). (2a) From this we then feed the sea surface temperature - the half the trend as the input to the Matsuno-Gill troposphere model representing 1958, (2b) and the temperature + half the trend as the input to the troposphere for 2017. The difference between the outputs of these two atmospheric models are taken to be the change that would have occurred if the model was run at every time step. (3) This wind stress trend is then turned into a wind stress anomaly by multiplying by the average wind speed from the ECMWF reanalysis product for each grid point using the formula $\Delta\vec{\tau} = C_d \rho_a W \Delta\vec{U}$ where $\Delta\vec{\tau}$ is the additional trend in wind stress computed from the $C_d$ is the drag coefficient, $\rho_a$ is the density of air, $W$ is the ECMWF average wind speed 1958-2017, $\Delta\vec{U}$ is the trend in the velocity from the atmosphere model. (4) The surface flux coefficients $\frac{dQ}{df}$ and $\frac{dQ}{dT}$ are calculated from the average sea surface temperature and the trend in sea surface temperature output from the ocean model. After this, the ocean model is run with the inputs from steps (3) and (4). The iterations are repeated for some number of iterations, $N$, (1)→(2)→(3)→(4)→(1).

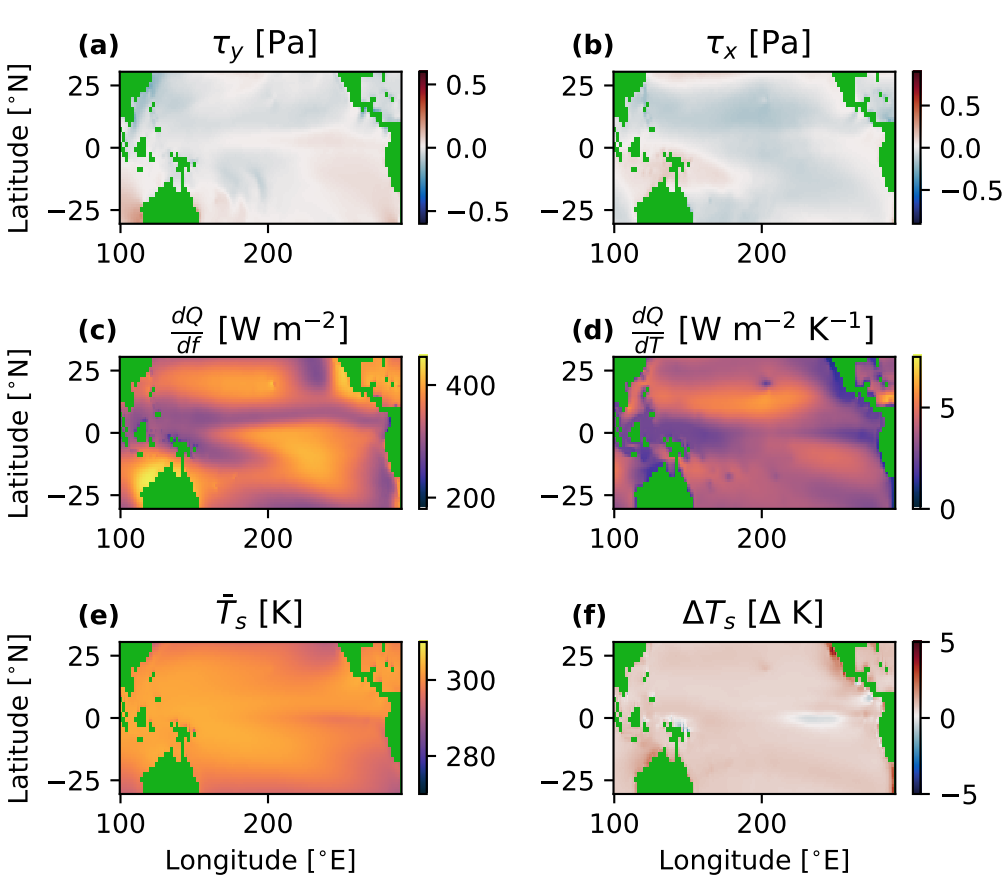


Figure 5: (a-f) Coupling fields passed from the troposphere (a & b), surface flux model (c & d), ocean model (e & f) for the final coupling iteration with the papers parameters, zoomed into the Equator, with the land values coloured green. (a & b) are the wind stresses from June-2007, where the majority of the sea surface trend have been added to the ECMWF wind stress for that month; (c) is the heat flux with increasing free energy; (d) is the heat flux with increasing temperature; (e) is the average temperature at each grid point; (f) is the change in the surface temperature.

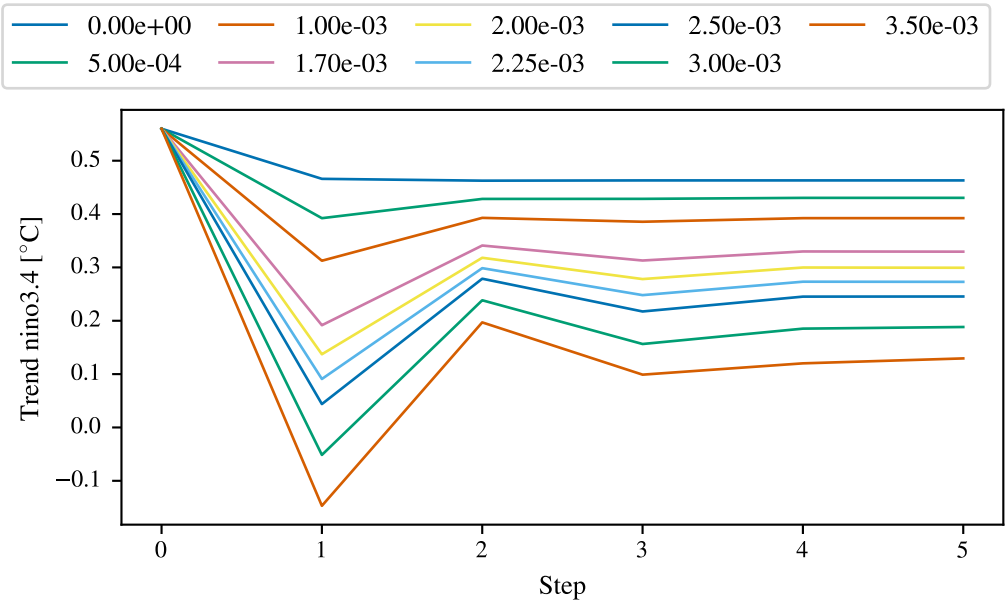


Simon D.A. Thomas

Figure 6: Trend in sea surface temperature over the nino3.4 region. Legend is the drag coefficient, $C_d$, of the run. The final step 4 → 5 changes the trend by less than 1%, and therefore this seems to be a reasonable stopping point.

# 4 Mechanism for the NINO3.4 Trend Bias

To recreate the model from S19 I use their parameters, as laid out in Table 3. In Table 4 I reproduce the experiments conducted in S19 with different sets of input fields: I find that I can reproduce the increase from swapping ECMWF out for CMIP5 multimodel mean (CMIP5-MMM) wind speed, and relative humidity, both together and independently (see Figure 7 for the inputs). For the experiments conducted the average increase in the nino3.4 trend caused by changing to CMIP5-MMM wind speed $\bar{W}$ is 0.054±0.05 K, changing to CMIP5-MMM relative humidity $\bar{r}$ leads to a 0.31±0.03 K change, and changing both together leads to a 0.47± K change. The errors are estimated by the range of points in experiments N, A, B, & C. This suggests that both the bias in CMIP5 relative humidity and wind speed lead to the observed cold tongue bias, and that they compound one another. The same effect is shown in each set of input parameters, suggesting that this effect is a robust feature of the model. However, the parameter settings given in the model produces an excessively high trend in nino3.4, and the S19 is more are more closely matched by the parameters in experiment C, where $\epsilon_v = 1/(9 \text{ hours})$ and $a = 0.6$, and does not vary due to deep convection.

The model is compared to the full results at every grid point given in the paper in Appendix F, and it reproduces the qualitative features of the model outputs (such as the value of the nino3.4 trend). However, there are some substantial differences, particularly in the width of the cold tongue feature, which appears to have more north-south extent in my implementation than in theirs. Given this, the following section investigates a substantially similar model to the model used in their paper, rather than identical. This highlights the problems with reproducibility that can arise when attempting to compress thousands of lines of code to a few lines in an appendix.

| Parameter | Value in paper | Units | Description |
|---|---|---|---|
| | | Cane-Zebiak [10] Ocean Model | |
| $\rho_w$ | 1023 | kg m$^{-3}$ | Density of water. |
| $\gamma$ | 0.75 | | Entrainment ratio of upwelling deep water. |
| $c_{pw}$ | 4184 | J kg$^{-1}$ | Heat capacity of water at constant pressure. |
| $H_s$ | 50 | m | Height of Ekman layer. |
| $H^*$ | 72.9 | m | Effective height of surface layer. |
| $r_E$ | 2 | day$^{-1}$ | Raleigh damping rate of Ekman motion. |
| $r_m$ | 3.5 | year$^{-1}$ | Raleigh damping rate of baroclinic modes. |
| $c_1$ | 2.98 | m s$^{-1}$ | Wave speed of first baroclinic mode. |
| $c_2$ | 1.85 | m s $^{-1}$ | Wave speed of second baroclinic mode. |
| | | Seager [15] Ocean Flux Model | |
| $\varepsilon$ | 0.97 | | Emmisivity of long wave radiation from Ocean. |
| $\sigma$ | $5.67\times10^{-8}$ | | Stefan-Boltzman constant |
| $C_E$ | 0.00125 | | Latent heat flux exchange coefficient. |
| $f_1$ | 0.39 | | 1st long wave flux parameter |
| $f_2$ | 0.05 | | 2nd long wave flux paramter. |
| $L$ | $2.5\times10^6$ | J kg−1 | Latent heat of evaporation of water. |
| $\delta T$ | 1 | K | Difference between SST and apparent surface air temp. |
| $r$ | 0.8 | | Constant relative humidity assumed in fixed model. |
| $T_{dc}$ | 28 | °C | Deep convection threshhold. |
| $a_{sc}$ | 0.8 | | Cloud constant $a$ if $T_s \leq 28$°C. |
| $a_{dc}$ | 0.4 | | Cloud constant $a$ if $T_s > 28$°C. |
| | | Matsuno-Gill Troposphere model | |
| $z_t$ | 15 | km | Height of the tropopause. |
| $\epsilon_u$ | 1/0.75 | day$^{-1}$ | Raleigh friction rate in $u$ direction. |
| $\epsilon_v$ | 1/1.5 | day$^{-1}$ | Raleigh friction rate in $v$ direction.* |
| $K$ | 1/10 | day$^{-1}$ | Newtonian cooling rate. |
| $N^2$ | $3 \times 10^{-4}$ | s$^{-2}$ | Buoyancy frequency. |
| $L$ | $2.5\times10^6$ | J kg−1 | Latent heat of evaporation of water. |
| $C_{pa}$ | 100 | J kg$^{-1}$ | Heat capacity of air at constant pressure. |
| $\bar{\rho}$ | 0.3 | kg m$^{-3}$ | Average density of the troposphere. |
| $\rho_{00}$ | 1.225 | kg m$^{-3}$ | Surface air density. |
| $H_q$ | 1,800 | m | Moisture scale. |
| | | Ocean-Troposphere coupling | |
| $C_d$ | 0.00225 | | Drag coefficient |

Table 3: Parameters as given in S19. * The only parameter for which the results data does not match S19 is $\epsilon_v$; $\epsilon_v = 1/(36$ hours) in the paper but $\epsilon_v = 1/(9$ hours) in the results data. As shown later in Table 4, the $\epsilon_v = 1/(9$ hours) value produces result more consistent with the paper's, and so this is may be a typographic error.

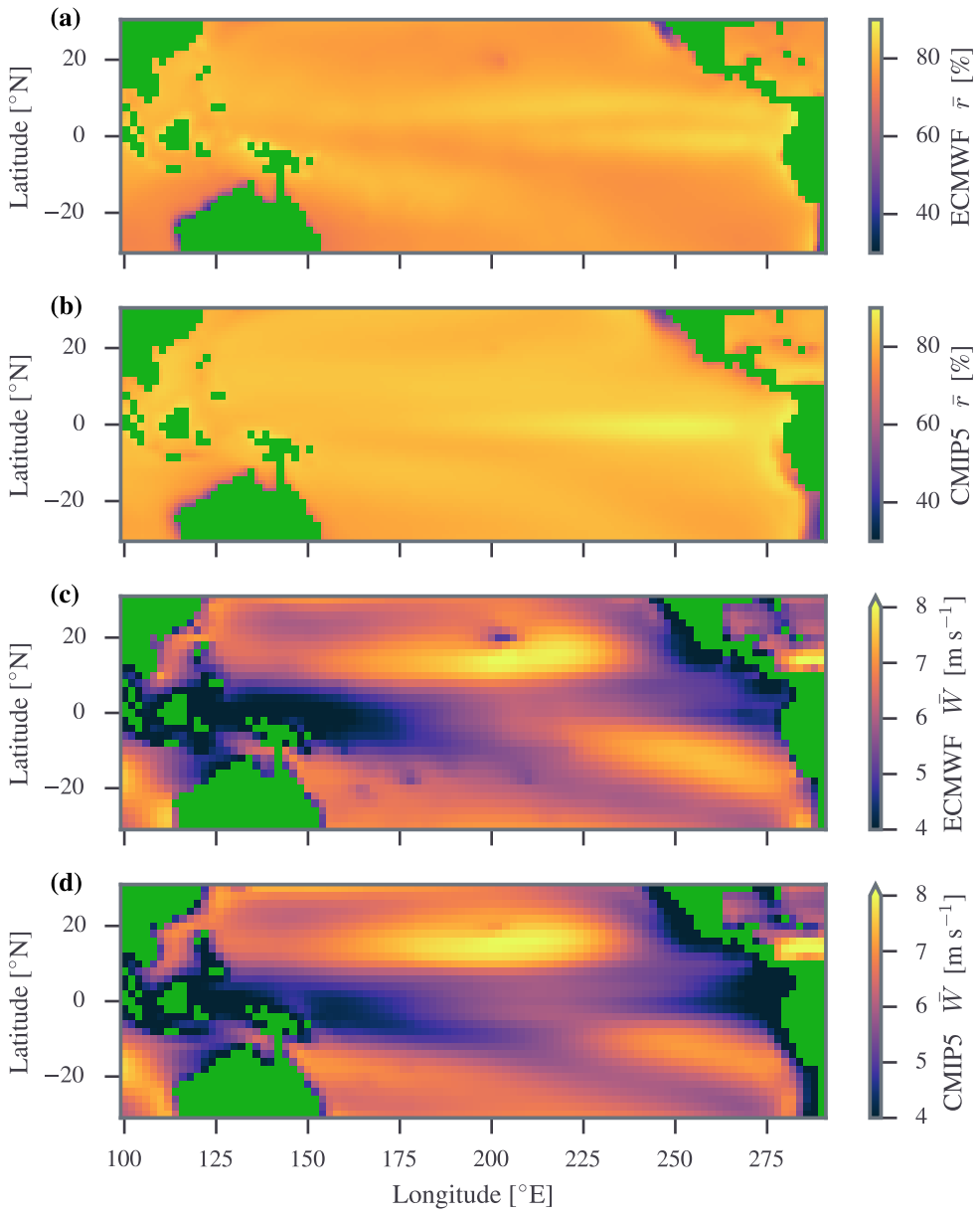


Figure 7: A comparison between the inputs from ECMWF (a & c) and CMIP5-MMM (b & d), for mean relative humidity, $\bar{r}$, (a & b), and the mean windspeed, $\bar{W}$, (a & b). (a & b) shows that the equator is too humid in CMIP5, (b & c) shows that there are insufficient tropical windspeeds in CMIP5.

| Type | Source | NINO3.4 trend [K] | | | | | | |
|---|---|---|---|---|---|---|---|---|
| | | **O** | **N** | **A** | **B** | **C** | **D** | **E** |
| R | HadlSST | 0.105 | | | | | | |
| R | NCEP/NCAR | 0.130 | | | | | | |
| R | ERSSTv5 | 0.352 | | | | | | |
| R | ECMWF/ORAS4 | 0.411 | | | | | | |
| S | CM-ECMWF world | 0.431 | 0.436 | 0.377 | 0.461 | 0.401 | 0.363 | 0.366 |
| S | CM-ECMWF F-RH | - | 0.455 | 0.398 | 0.475 | 0.416 | 0.364 | 0.380 |
| S | CM-ECMWF C-W | - | 0.492 | 0.428 | 0.522 | 0.452 | - | - |
| S | CM-ECMWF C-RH | 0.678 | 0.783 | 0.646 | 0.828 | 0.686 | 0.578 | 0.617 |
| S | CM-ECMWF C-RH W | 0.832 | 0.948 | 0.780 | 1.002 | 0.827 | - | - |
| S | CM-CMIP5 world | 0.865 | | | | | | |
| C | CMIP5 multimodel mean | 0.889 | | | | | | |

Table 4: A comparison of the different projection for the trend in nino3.4 over the 60 year period up to 2017. The data was extracted from Figure 1. The types are R=Reanalysis product, S=S19 type model experiment, C=CMIP5. 'CM-ECMWF' world has all inputs from ECMWF; 'CM-ECMWF C-RH' uses the CMIP5 multimodel mean relative humidity; 'CM-ECMWF C-RH W' uses the CMIP5 multimodel mean relative humidity and wind speed; 'CM-ECMWF F-RH' uses a fixed value for the relative humidity. O represents the actual value extracted from Figure 1. N, A, B, C, D and E record different model experiments I conducted, listed in Table 5.

| Experiment | $a$ varies | Value of the cloud constant, $a$ | Quadruple $\epsilon_v$ | $1/\epsilon_v$ timescale |
|---|---|---|---|---|
| N | True | $a = 0.4$ if $T_s > 28°$C, $a = 0.8$ if $T_s \leq 28°$C | False | $1/\epsilon_v = 32$ hours |
| A | False | $a = 0.6$ | False | $1/\epsilon_v = 32$ hours |
| B | True | $a = 0.4$ if $T_s > 28°$C, $a = 0.8$ if $T_s \leq 28°$C | True | $1/\epsilon_v = 9$ hours |
| C | False | $a = 0.6$ | True | $1/\epsilon_v = 9$ hours |
| D | False | $a = 0.4$ | False | $1/\epsilon_v = 32$ hours |
| E | False | $a = 0.4$ | True | $1/\epsilon_v = 9$ hours |

Table 5: Model experiments used in Table 4. The Raleigh damping timescale in the opposite direction stays at a constant 1/(0.75 days) or 1/(18 hours).

# 5 Sensitivity analysis

## 5.1 Methodology

When conducting sensitivity analyses, it is standard practice to have a probability distribution over the input parameters and look to propagate those onto the output parameter. This allows it be ascertained how the errors in the parameters contribute the most to the final error, and how they compound.

However, given that the parameters used in this model are mostly unmeasurable, and made to tune the idealised model, the specification of a probability distribution over them would have been uninformed guesswork. Instead, I look to try to calculate the local gradient of the output (in this case the trend in sea surface temperature in certain regions, that varying a parameter produces). The following sections use the C parameter settings for the 'CM-ECMWF F-RH' experiment (see Table 5).

## 5.2 Varying the Drag Coefficient

The most obvious variable to change is $C_d$ as the paper notes that the value that they used, $2.25\times10^{-3}$, is substantially larger than the value of $1.75\times10^{-3}$ typically used in such a model [2]. Figures 9a & 9b, show the change in two regions of the model. In the nino3.4 region, we see a linear decrease in the trend as the drag coefficient is decreased, showing that as expected the anomaly applied from the atmosphere has the effect of strengthening upwelling at the equator. The response is more complicated in the nino1+2 trend (Figure 9b).

## 5.3 Varying the Raleigh Friction Rate

We can vary the timescale that the velocities decay over, measured in days. In the paper $1/\epsilon_u = 2/\epsilon_v = 0.75$ days, which means that the rate of decay in the $u$ wind is twice as strong as the $v$ wind. Figure 10 shows the complicated, non-linear pattern that varying both together produces. Romps 2014 [20] was able to vary the coefficient up to 10 days, but I found that the model would break down above about 2.5 days, as nan values from excessive wind stress forcing would spread through the ocean model. Figure 5.4 shows how the Raleigh friction alters the ocean overall, producing a similar pattern to varying $c_d$, likely as both act through the same mechanism of increasing the wind stress anomaly that is added to the ECMWF reanalysis product and forces the ocean model.

## 5.4 Varying the Newtonian Cooling Rate

The Newtonian cooling term for the paper is that $\frac{1}{K} = 10$ days, which identical to Bretherton & Sobel 2003 [21] which they see as a way to impose the weak temperature gradient approximation [22]. This parameter is varied independently in Figure 13, the relationship quickly becomes non-linear, and so I fit the the a linear model to the values between 7 and 14 days to measure the local gradient $(1.2 \pm 0.2) \times 10^{-2}$ K day$^{-1}$.

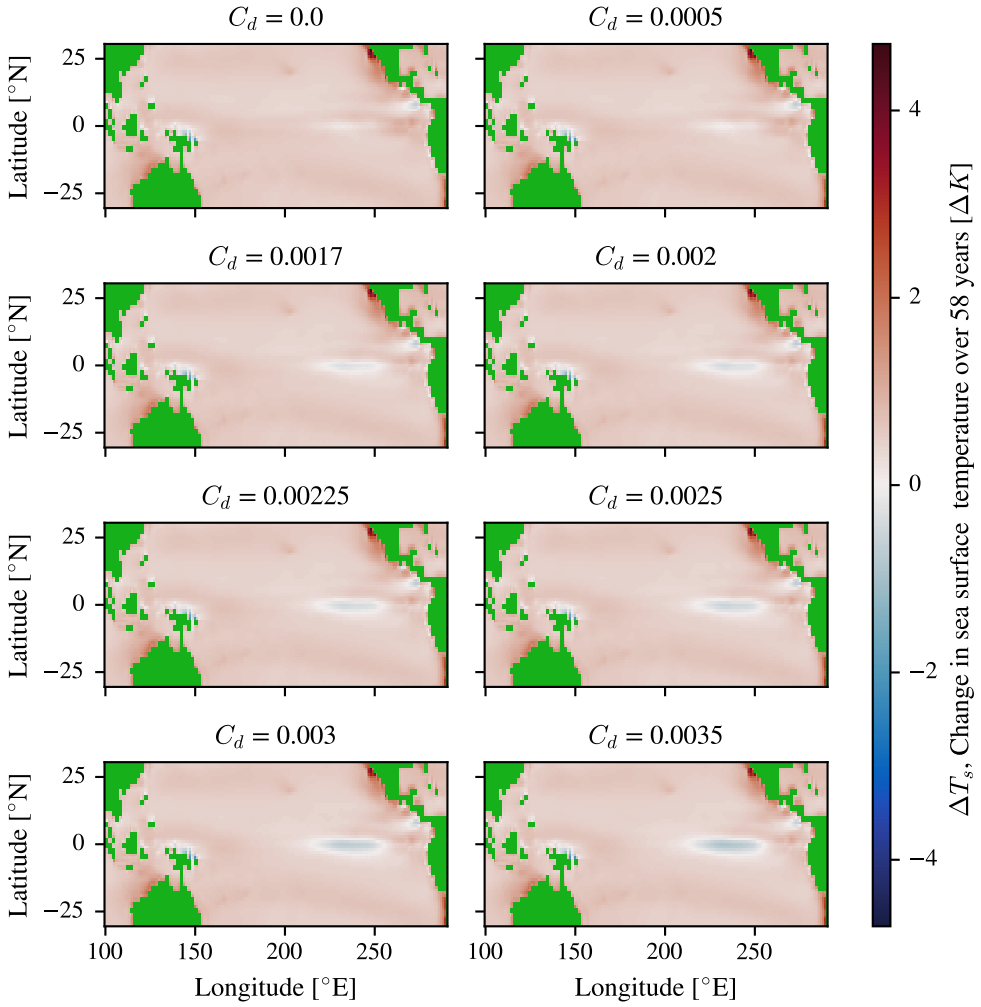


(a) I varied the drag coefficient, $C_d$, between the above values. The cold tongue feature gradually expands in size, as a larger westward wind stress anomaly is added. The errors are calculated according to Appendix B, using standard methods for linear regression, with the assumption that the errors in the parameters are Gaussian and independent.
(b) The linear trend between the above stress levels. This highlights that increasing the drag coefficients cools the cool tongue around the equator, but leads to some anomalous heating off the coast of Peru and Chile.

Figure 8: The drag coefficient is varied between the values in Figure 8a, and Figure ?? is the linear fit between these values for each grid point.

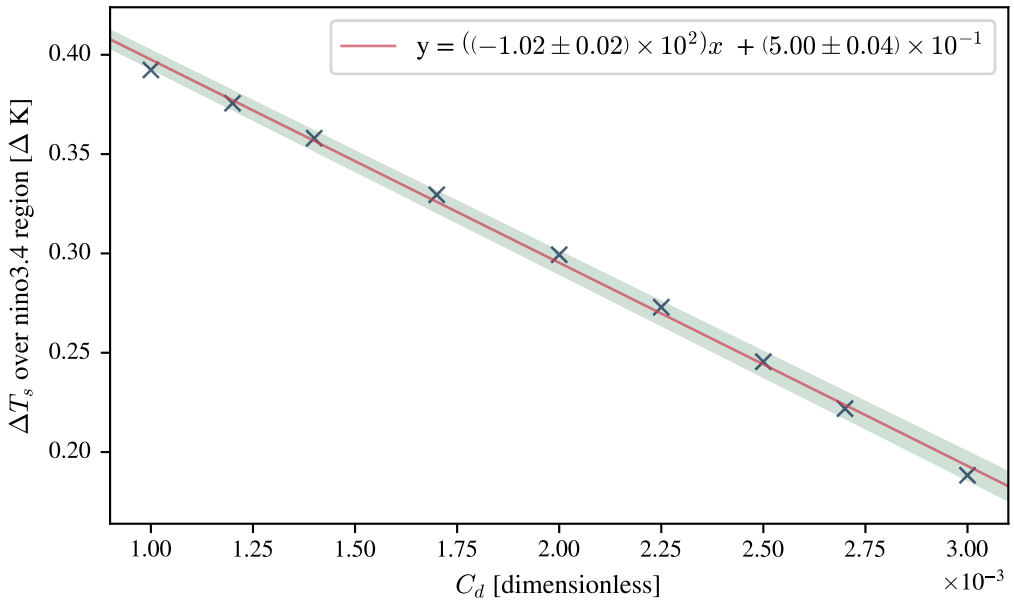


(a) The trend in the sea surface temperature in the `nino3.4` region from the coupled model, as the drag coefficient is changed. The sensitivity is well modelled by a linear trend, with relatively tight error bars exceeded by roughly a third of the data points, although points are more likely to be below the trend line at the low and high drag coefficient, showing that there is some measurable curvature to the relationship.

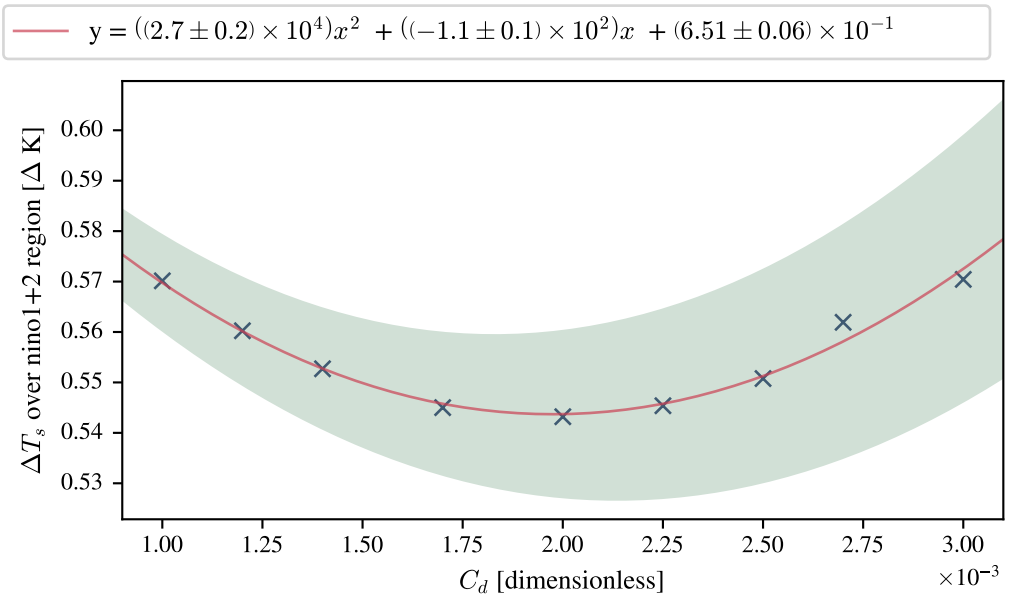


(b) The trends over the `nino1+2` region as the drag coefficient, $C_d$, changes. We see that the trend reaches a minima at roughly $C_d = 2.0 \pm 0.1$. We can see from Figure ?? that this could arise from a competition between decreased upwelling off the coast of Peru, and the increased upwelling over the cold tongue, whilst $C_d$ is increased.

Figure 9: The drag coefficient is varied, and changes the trend in different average nino regions in the sea surface temperature of the model.

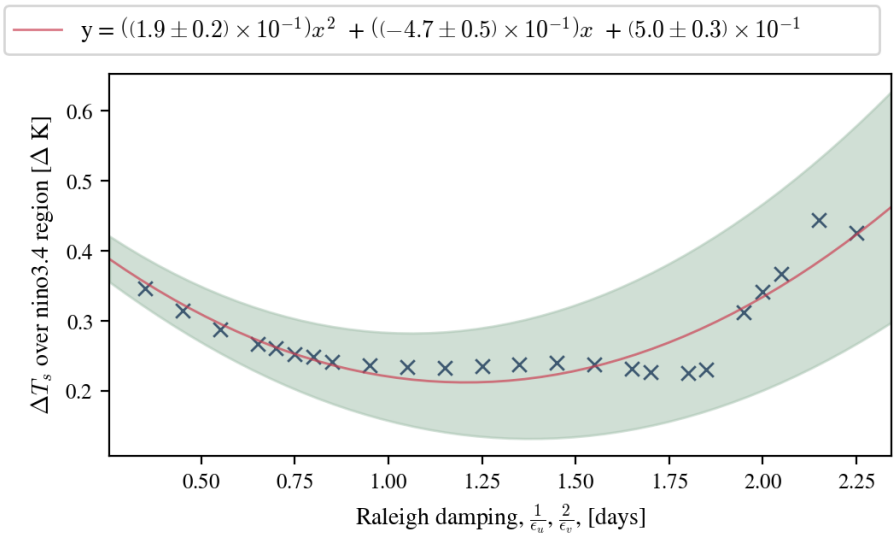


Figure 10: A facet plot with the different values of $\frac{1}{\epsilon_u}$. As the timescale of the drag coefficient is increased, the trend in nino3.4 around 0.75 days initially decreases as the wind speed increases over the central Pacific to increase upwelling but at higher values, the trend first plateaus above 1.75 days, and then begins to increase, and becoming increasingly unstable above 2 days, and eventually the model breaks down entirely above 3 days. The parabola does not fit the data well, hence the error bars are poorly calibrated. A higher move flexible Gaussian process model would be more helpful.

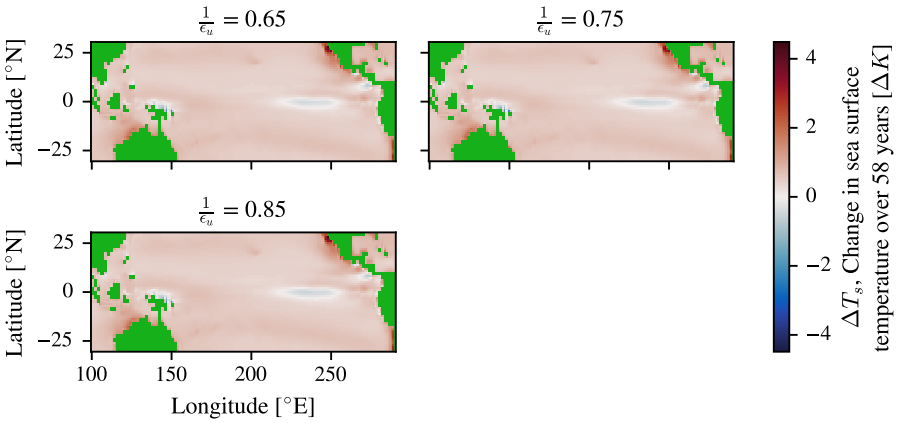


Figure 11: A facet plot with the different values of $\frac{1}{\epsilon_u}$ around the paper's value of $\frac{1}{\epsilon_u} = 0.75$ days, so that the trend will be locally linear.

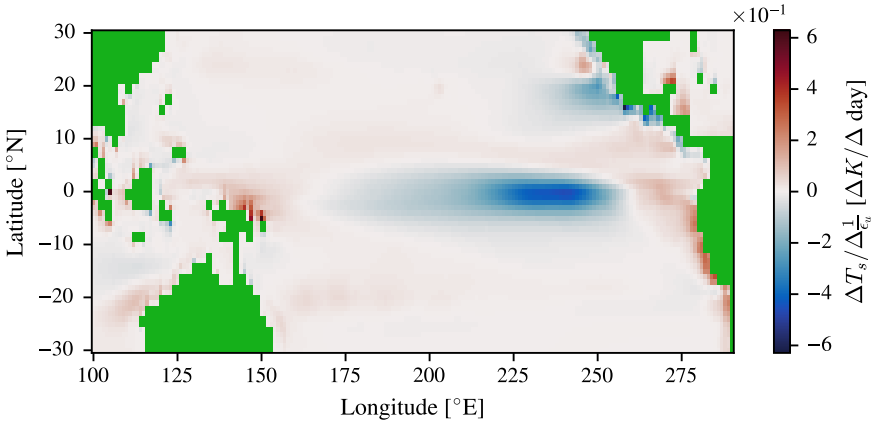


Simon D.A. Thomas

Figure 12: The linear trend fitted between these three points, showing that the increase in the timescale. It is substantially similar to the sensitivity shown in Figure ??.

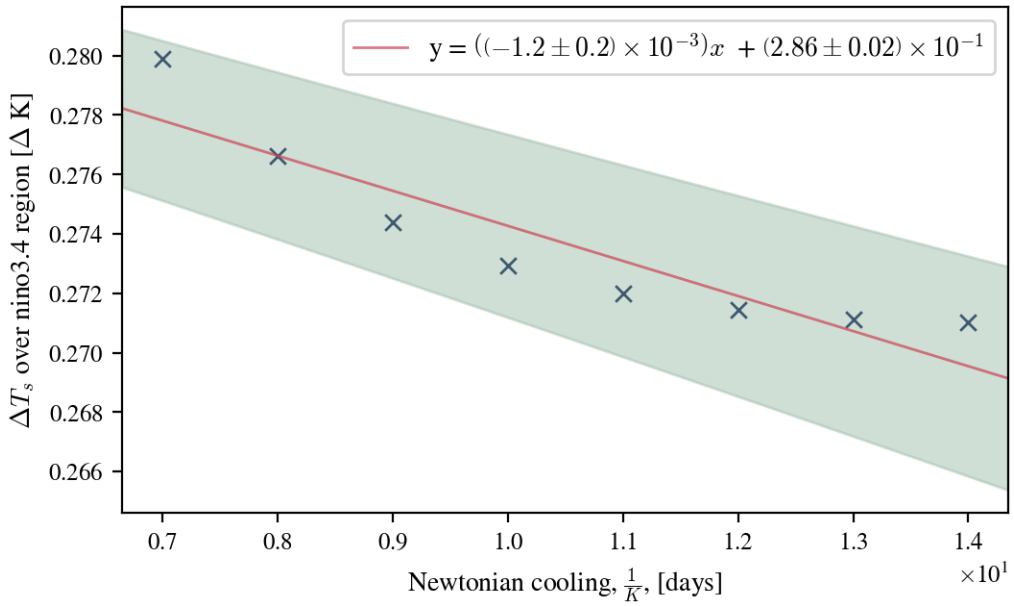


Figure 13: Varying the Newtonian cooling timescale $\frac{1}{K}$, leads to slightly different trends in the nino3.4 region, although the difference is only between about 0.28 and 0.27 between 7 and 14 days, suggesting that this does not effect the nino3.4 balance substantially.

# 6 Discussion and Further Work

In Section 4 I showed that the coupled model can reproduce the CMIP5-MMM bias when CMIP5-MMM values for wind speed, $W$, and relative humidity, $r$, are used as inputs to the model. However, the CMIP bias may be overdetermined. The coupled model still takes an input of the average precipitation $\bar{P}_r$, its trend $\Delta P_r$, and the surface pressure $p_s$ from the ECMWF reanalysis product. It is possible that if these variables were swapped out for their corespondent CMIP5-MMM values that the $\Delta T_s$ in nino3.4 could change so that it is no longer in agreement with the CMIP5-MMM values.

In Section 5 I showed that the model shows varying levels of sensitivity of the nino3.4 region to the variation of the parameters tested. As the drag coefficient, $C_d$ is varied the gradient in the trend in nino3.4 is $(-1.02 \pm 0.02) \times 10^2$ K, and can vary by 0.2 $K$ or 50% in the plotted range. As the Raleigh friction in the troposphere, $\frac{1}{\epsilon_u} = \frac{2}{\epsilon_v}$ is varied the gradient in the trend in nino3.4 around the paper's value is $-(3.3 \pm 0.5) \times 10^{-1}$ K day$^{-1}$, and can vary by 0.2 K or 50% in the plotted range. As the Newtonian cooling, $\frac{1}{K}$, is varied locally around the paper's value, the gradient in the trend in nino3.4 is $(1.2 \pm 0.2) \times 10^{-2}$ K day$^{-1}$, and it can vary by 0.01 K in the plotted range, or less than 1%.

This suggests that the model is tuneable in its agreement with ECMWF/ORAS4. There are also a large number of other parameters that could be changed (see Table 3), and so the sensitivity of the model to these is unknown. A downside of using a simplified model is that some or many of the parameters in question have no obvious observational or experimental constraint.

This model only uses linear dynamics and relies on the ECMWF reanalysis product for forcing. It is dissimilar from CMIP5 models are able to resolve a large number of complex non-linear interactions. Therefore is unclear whether the mechanisms that affect our model, will act in the same way in the CMIP models, and therefore that the mechanism is valid. Given this type of linear model's use in the previous literature, we can be confident that it does capture the important processes, such as the propagation of Kelvin waves [10, 13], that occur around the equator. However, the ENSO oscillations within the model are unrealistic, due to a coupling time of 60 years between the ocean and atmospheric components. ENSO is an intrinsically coupled phenomena, and so it would improve the model if we were to couple the simple models together at every time step (which is work currently being carried out by Dr. Hanghoi Zhang).

Further work could include testing how biased CMIP6 is compared in the same period. The higher resolutions used in CMIP6, and additional processes included, may change the details of the bias (although it still exists [23]). The bias in the state of ENSO could also be directly tracked onto an error in the number and intensity of tropical cyclones (see Appendix A), so that a bias in the risk could be calculated. The proposed mechanism of why this ENSO bias occurs may help future model development to lead to better convection schemes. In the meantime bias correction schemes should be careful as to how they ensure that the ENSO bias, which is likely to be non-stationary (Appendix C), is corrected.

# 7 Conclusion

The coupled physical model used in this report provides a plausible mechanism for why the CMIP5 models get the trend in the surface temperature over the NINO3.4 region of the central Pacific wrong. The bias could be caused by the compound of a bias in the relative humidity and wind speed fields. This mechanism is robust to substantial changes in the model's parameters. The coupled physical model, which is substantially similar to that used in S19, is relatively insensitive to the parameters chosen, in that it would it will stay within an observed nino3.4 trend of $0.3 \pm 0.1$ °C whilst the free parameters tested in this study are varied, in rough agreement with the trend from the ECMWF/ORAS4 reanalysis product. Therefore, this would suggest that as far as tested the model used in S19 is relatively robust, and its conclusions as to the mechanism behind this are believable. The model reassembled here should be easy to use, and relatively cheap to run, at 1 hour 20 for the 6 coupling iteration setup is shown. Therefore, it may be an interesting pedagogical resource.

## Acknowledgements

Thanks is due to: Dr. Dan Jones for excellent supervision; Dr. Naomi Henderson who wrote the model for S19, and left the uncoupled version of the code online for me to use[2], and who met with me and answered my foolish questions; Dr. s John Talyor and Michael Herzog, who provided useful questions to address at the beginning of the project; Dr. Hanghoi Zhang who provided pointers on how to get the model to work; Dr. Adam Sobel whose useful podcast introduced me to the paper in the first place.[3]

## References

1. Cane, M. A. *et al.* Twentieth-century sea surface temperature trends. *Science* **275,** 957–960. ISSN: 00368075. doi:10.1126/science.275.5302.957. http://science.sciencemag.org/ (Feb. 1997).
2. Seager, R. *et al.* Strengthening tropical Pacific zonal sea surface temperature gradient consistent with rising greenhouse gases. *Nature Climate Change* **9,** 517–522. ISSN: 17586798. doi:10.1038/s41558-019-0505-x. https://doi.org/10.1038/s41558-019-0505-x (July 2019).
3. Zhang, G. J., Song, X. & Wang, Y. *The double ITCZ syndrome in GCMs: A coupled feedback problem among convection, clouds, atmospheric and ocean circulations* Nov. 2019. doi:10.1016/j.atmosres.2019.06.023.
4. Patricola, C. M., Saravanan, R. & Chang, P. The impact of the El Niño-Southern oscillation and Atlantic meridional mode on seasonal Atlantic tropical cyclone activity. *Journal of Climate* **27,** 5311–5328. ISSN: 08948755. doi:10.1175/JCLI-D-13-00687.1. https://journals.ametsoc.org/view/journals/clim/27/14/jcli-d-13-00687.1.xml (July 2014).
5. Camargo, S. J., Emanuel, K. A. & Sobel, A. H. Use of a genesis potential index to diagnose ENSO effects on tropical cyclone genesis. *Journal of Climate* **20,** 4819–4834. ISSN: 08948755. doi:10.1175/JCLI4282.1. https://journals.ametsoc.org/view/journals/clim/20/19/jcli4282.1.xml (Oct. 2007).
6. Quan, M., Wang, X., Zhou, G., Fan, K. & Zikang, H. Effect of winter-to-summer El Niño transitions on tropical cyclone activity in the North Atlantic. **54,** 1683–1698. doi:10.1007/s00382-019-05081-9. https://doi.org/10.1007/s00382-019-05081-9 (2020).
7. Bjerknes, J. Atmospheric Teleconnections from the Equatorial Pacific. *Monthly Weather Review* **97,** 163–172. doi:10.1175/1520-0493(1969)097<0163:ATFTEP>2.3.CO;2. https://journals.ametsoc.org/view/journals/mwre/97/3/1520-0493_1969_097_0163_atftep_2_3_co_2.xml (1969).
8. Cane, M. A., Zebiak, S. E. & Dolan, S. C. Experimental forecasts of EI Nino. *Nature* **321,** 827–832. doi:10.1038/321827a0. https://doi.org/10.1038/321827a0 (June 1986).
9. Cushman-Roisin, B. & Beckers, J.-M. *Introduction to Geophysical Fluid Dynamics2nd Edition* 2nd ed. ISBN: 9780120887590. https://www.elsevier.com/books/introduction-to-geophysical-fluid-dynamics/cushman-roisin/978-0-12-088759-0 (Academic Press, Aug. 2011).
10. Cane, M. A. Modeling Sea Level During El Niño in. *Journal of Physical Oceanography* **14,** 1864–1874. https://journals.ametsoc.org/view/journals/phoc/14/12/1520-0485_1984_014_1864_mslden_2_0_co_2.xml (Dec. 1984).

[2] http://kage.ldeo.columbia.edu:81/SOURCES/.LDEO/.ClimateGroup/.PROJECTS/.PublicationsData/.Seager_etal_NCC-2019/ (this domain is blocked when using the Cambridge VPN)

[3] https://deep-convection.org/2020/04/13/episode-5-richard-seager/ paper specifically discussed 33:00-44:30.

11. Blumenthal, M. B. & Cane, M. A. Accounting for Parameter Uncertainties in Model Verification: An Illustration with Tropical Sea Surface Temperature in: Journal of Physical Oceanography Volume 19 Issue 6 (1989). *Journal of Physical Oceanography* **19.** https://journals.ametsoc.org/view/journals/phoc/19/6/1520-0485_1989_019_0815_afpuim_2_0_co_2.xml?tab_body=pdf (1989).
12. Seager, R. A Simple Model of the Climatology and Variability of the Low-Level Wind Field in the Tropics. *Journal of Climate* **4,** 164–179. doi:10.1175/1520-0442(1991)004<0164:ASMOTC>2.0.CO;2. https://journals.ametsoc.org/view/journals/clim/4/2/1520-0442_1991_004_0164_asmotc_2_0_co_2.xml (1991).
13. Zebiak, S. E. & Cane, M. A. A Model El Niño–Southern Oscillation. *Monthly Weather Review,* 2262–2278. https://journals.ametsoc.org/view/journals/mwre/115/10/1520-0493_1987_115_2262_ameno_2_0_co_2.xmlhttps://doi.org/10.1175/1520-0493(1987)115<2262:AMENO>2.0.CO;2 (Oct. 1987).
14. Cane, M. A. & Zebiak, S. E. A theory for El Niño and the Southern Oscillation. *Science* **228,** 1085–1087. ISSN: 00368075. doi:10.1126/science.228.4703.1085. http://science.sciencemag.org/ (May 1985).
15. Seager, R., Blumenthal, M. B. & Kushnir, Y. An Advective Atmospheric Mixed Layer Model for Ocean Modeling Purposes. *Journal of Climate* **8,** 1951–1964. https://www.jstor.org/stable/26200030 (Aug. 1995).
16. Israeli, M., Naik, N. H. & Cane, M. A. An Unconditionally Stable Scheme for the Shallow Water Equations in. *Monthly Weather Review* **128.** doi:10.1175/1520-0493(2000)128<0810:AUSSFT>2.0.CO;2. https://journals.ametsoc.org/view/journals/mwre/128/3/1520-0493_2000_128_0810_aussft_2.0.co_2.xml (2000).
17. Matsuno, T. Quasi-Geostrophic Motions in the Equatorial Area. *Journal of the Meteorological Society of Japan,* 25–43. doi:10.2151/jmsj1965.44.1{_}25. https://www.jstage.jst.go.jp/article/jmsj1965/44/1/44_1_25/_article (Feb. 1966).
18. Gill, A. E. Some simple solutions for heat-induced tropical circulation. *Quaterly Journal of the Royal Meteorologcal Society* **106,** 447–462. doi:10.1002/qj.49710644905 (1980).
19. Seager, R., Kushnir, Y. & Cane, M. A. On Heat Flux Boundary Conditions for Ocean Models. *Journal of Physical Oceanography,* 3219–3230. https://journals.ametsoc.org/view/journals/phoc/25/12/1520-0485_1995_025_3219_ohfbcf_2_0_co_2.xmlhttps://doi.org/10.1175/1520-0485(1995)025<3219:OHFBCF>2.0.CO;2 (Dec. 1995).
20. Romps, D. M. Rayleigh damping in the free troposphere. *Journal of the Atmospheric Sciences* **71,** 553–565. ISSN: 00224928. doi:10.1175/JAS-D-13-062.1. https://journals.ametsoc.org/view/journals/atsc/71/2/jas-d-13-062.1.xml (Feb. 2014).
21. Bretherton, C. S. & Sobel, A. H. The Gill Model and the Weak Temperature Gradient Approximation. *Journal of the Atmospheric Sciences* **60,** 451. https://journals.ametsoc.org/view/journals/atsc/60/2/1520-0469_2003_060_0451_tgmatw_2.0.co_2.xmlhttps://doi.org/10.1175/1520-0469(2003)060<0451:TGMATW>2.0.CO;2 (Jan. 2003).
22. Sobel, A. H., Nilsson, J. & Lorenzo, M. P. The Weak Temperature Gradient Approximation and Balanced Tropical Moisture Waves. *Journal of the Atmospheric Sciences,* 3650–3665. https://journals.ametsoc.org/view/journals/atsc/58/23/1520-0469_2001_058_3650_twtgaa_2.0.co_2.xmlhttps://doi.org/10.1175/1520-0469(2001)058<3650:TWTGAA>2.0.CO;2 (Dec. 2001).
23. Tian, B. & Dong, X. The Double-ITCZ Bias in CMIP3, CMIP5, and CMIP6 Models Based on Annual Mean Precipitation. *Geophysical Research Letters* **47,** e2020GL087232. ISSN: 0094-8276. doi:10.1029/2020GL087232. https://onlinelibrary.wiley.com/doi/abs/10.1029/2020GL087232 (Apr. 2020).

24. Bister, M. & Emanuel, K. A. Low frequency variability of tropical cyclone potential intensity 1. Interannual to irtterdecadal variability. *Journal of Geophysical Research Atmospheres* **107,** 26–1. ISSN: 01480227. doi:10.1029/2001JD000776 (2002).

25. Camargo, S. J. & Wing, A. A. Tropical cyclones in climate models. *Wiley Interdisciplinary Reviews: Climate Change* **7,** 211–237. ISSN: 17577780. doi:10.1002/wcc.373. http://doi.wiley.com/10.1002/wcc.373 (Mar. 2016).

26. Tang, B. & Emanuel, K. A ventilation index for tropical cyclones. *Bulletin of the American Meteorological Society* **93,** 1901–1912. ISSN: 00030007. doi:10.1175/BAMS-D-11-00165.1. http://dx.doi.org/10.1175/BAMS-D-11-00165.2 (Dec. 2012).

27. Hoogewind, K. A., Chavas, D. R., Schenkel, B. A. & O'Neill, M. E. Exploring controls on tropical cyclone count through the geography of environmental favorability. *Journal of Climate* **33,** 1725–1745. ISSN: 08948755. doi:10.1175/JCLI-D-18-0862.1. www.ametsoc.org/PUBSReuseLicenses (Mar. 2020).

28. Camargo, S. J., Tippett, M. K., Sobel, A. H., Vecchi, G. A. & Zhao, M. Testing the performance of tropical cyclone genesis indices in future climates using the HiRAM model. *Journal of Climate* **27,** 9171–9196. ISSN: 08948755. doi:10.1175/JCLI-D-13-00505.1. https://journals.ametsoc.org/view/journals/clim/27/24/jcli-d-13-00505.1.xml (Dec. 2014).

29. Virtanen, P. *et al.* SciPy 1.0: fundamental algorithms for scientific computing in Python. *Nature Methods* **17,** 261–272. ISSN: 15487105. doi:10.1038/s41592-019-0686-2. https://doi.org/10.1038/s41592-019-0686-2 (Mar. 2020).

30. Lebigot, E. O. *Uncertainties: a Python package for calculations with uncertainties* 2016. https://pythonhosted.org/uncertainties/.

# A Exploring the Global Bias in the Risk of Tropical Cylones

Future work will hopefully involve seeing if this same bias exists in CMIP6, and what its effect could be. The potential intensity of tropical cyclones is accepted as being well captured by an idealised Carnot engine running between the sea surface and the Tropopause (e.g. [24]). There is less consensus about the best way to predict the frequency of tropical cyclones [25], A common ventilation was suggested in [26]. A practical paper [27] uses absolute vorticity. Camargo et al. 2014 [28] shows that mid-level saturation deficit may be superior to mid-level relative humidity. Rather than deciding between these different indices, it could be enough to show that their is a statistical difference in each.

# B Polynomial Regression and Error Propagation

`scipy` allows curves to be fitted by least squares, and returns the covariance matrix in the optimisation towards the parameters. An estimation of the uncertainty in each of the parameters can be found as the square root of the diagonal entries of this matrix [29]. This ignores the part of the correlation matrix which is the correlation between the different parameters, and assumes that their values are all independent. This will be increasingly significant as more parameters are fitted to the model. However, given that it is more common and interpretable to look at the error in an individual variable, and more easy to communicate it, it seems that the plot should match the reported model parameters, rather than being more accurate.

The assumptions made when fitting the linear trends will not actually be satisfied by the time series within this report, as the long timescale oscillations caused by for example the El Niño Southern Oscillation mean that the data is not identically and independently distributed. Given this the errors calculated by the normal methods will also be based on flawed assumptions, but they are included as a rough guide to the

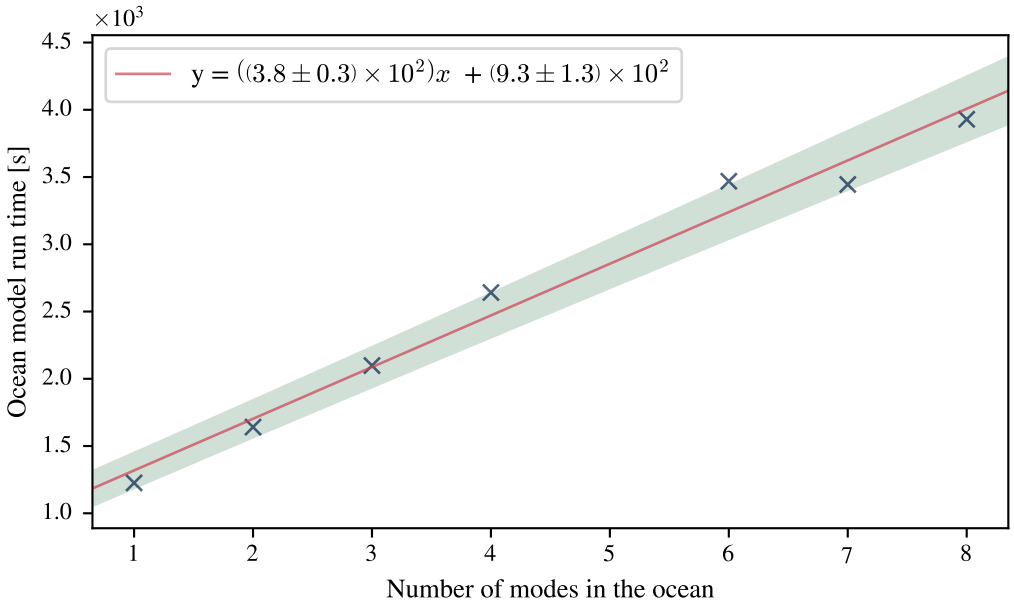


Figure 14: The computational cost of the ocean model in seconds of run time for the main 58 years of model run in terms of the number of seconds it takes to run on a particular machine (`jasmin-sci2`). increases by around 6:20 minutes for each additional mode. The original model used 2 modes. The trend line, and its associated $1\sigma$ error bar is calculated while assuming the errors in the parameters are Gaussian and independent.

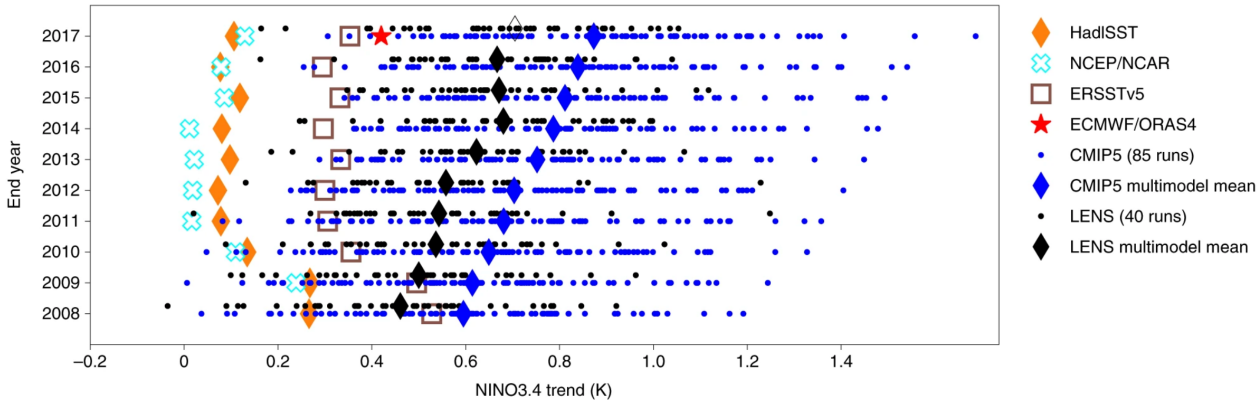


Figure 15: Figure 1(g) from S19: The temperature anomaly trend, $\Delta T_s$ in the nino3.4 box (190 to 240°E, −5 to 5°N) for the last 60 years up to the end year. The blue points represent the CMIP5 historical ensemble members, and the black points represent the LENS ensemble members, with their respective diamonds representing their multimodel mean. This red star is the ECMWF-ORAS4 model, from which the input fields were taken to drive the coupled model in S19, which runs from 1957-2017.

approximate uncertainty in the trend, rather than an exact result. They are merely 'better than nothing', so that the reader has some guide as to whether the difference between different values is significant.

Given that these parameters now have symmetric errors around them, this error can be propagated according to linear uncertainty propagation theory with the `uncertainties` [30] python package, through the automatic calculation of the gradient of the function. This then allows to the error to be propagated from the $x$ input at any point to the $y$ output, and therefore for the predictions to be given as probabilistic one standard deviation envelopes. The reader may assume that I am plotting a Gaussian Process (GP), given the visual similarity of the graph style, but I chose not to because I found these polynomial fits to be more interpretable and parsimonious, as they output a few parameter with a physical meaning and an approximate uncertainty. An example of doing this is given in Figure 14, where I vary the number of baroclinic modes in the model of the ocean on the same computer, and see how much longer it takes for the model to run. This results in a fair fit with a reasonable error bar produced.

# C Non-stationarity of ENSO bias

In Figure 15 we can see the change in the trend of `nino3.4` trends over the 60 years ending in the final year on the $y$ axis. You can see that the reanalyses products show a small or nonexistent trend, whereas the CMIP ensemble members universally show a positive trend during the historical period. The difference between the two appears to grow during time, although only a small range of end years are chose. This trend changes over time, suggesting some level of non-stationarity, that will ultimately make forms of statistical bias correction more difficult to accomplish.

# D Word count

The word count is given here:

```
File: main.tex
```

Simon D.A. Thomas

```
Encoding: ascii
Sum count: 4961
Words in text: 3373
Words in headers: 52
Words outside text (captions, etc.): 1386
Number of headers: 18
Number of floats/tables/figures: 13
Number of math inlines: 127
Number of math displayed: 23
Subcounts:
  text+headers+captions (#headers/#floats/#inlines/#displayed)
  0+0+0 (1/0/0/0) _top_
  433+1+162 (1/2/2/0) Section: Introduction
  296+8+90 (1/1/1/0) Section: The Tropical Pacific and El Ni\~no Southern Oscillation
  0+2+0 (1/0/0/0) Section: Physical model
  327+3+8 (1/0/26/3) Subsection: Common Model Features
  280+1+0 (1/0/19/4) Subsection: Ocean
  256+8+0 (3/0/12/14) Subsection: Atmosphere
  342+1+465 (1/3/22/2) Subsection: Coupling
  317+6+221 (1/3/13/0) Section: Mechanism for the NINO3.4 Trend Bias
  0+2+0 (1/0/0/0) Section: Sensitivity analysis
  125+1+0 (1/0/0/0) Subsection: Methodology
  90+4+0 (1/0/3/0) Subsection: Varying the Drag Coefficient
  126+5+0 (1/0/4/0) Subsection: Varying the Raleigh Friction Rate
  62+5+440 (1/4/10/0) Subsection: Varying the Newtonian Cooling Rate
  538+4+0 (1/0/14/0) Section: Discussion and Further Work
  181+1+0 (1/0/1/0) Section: Conclusion
```

# E Documentation

The documentation for the project's code is appended after this page. For an interactive version visit https://seager19.readthedocs.io/.

# F Replication of S19 Figures

See replication of S19 figures after this page.

seager-rep

July 12, 2021

# 1 Checking consistency between S19 figures and model output

[1]:
```
# Convenient jupyter setup
%load_ext autoreload
%autoreload 2
%config IPCompleter.greedy=True
```

[33]:
```
# set up plotting settings for dark mode.
from jupyterthemes import jtplot
jtplot.style(theme="grade3", context="notebook", ticks=True, grid=False)
from src.plot_utils import ps_defaults
ps_defaults(use_tex=False, dpi=150)
```

[34]:
```
# general packages
import os
import xarray as xr
import matplotlib.pyplot as plt
```

[162]:
```
# Get the helper functions
from src.models.model_setup import ModelSetup
from src.xr_utils import open_dataset, open_dataarray, get_trend, clip,␣
 ↪can_coords, sel
from src.utils import get_default_setup
from src.configs.load_config import load_config
from src.plot_utils import add_units, cmap, get_dim, label_subplots
from src.constants import UC_LOGS, FIGURE_DATA_PATH, FIGURE_PATH
from src.wandb_utils import setup_from_name
from src.visualisation.comp import comp_oc_sst, comp_atm_prwnd, comp_oc_htherm,␣
 ↪return_figure_ds
uncoupled_run_dir = str(UC_LOGS / "it_1")
cfg = load_config(test=False)
fig_data = xr.open_dataset(FIGURE_DATA_PATH)
uncoup_setup = ModelSetup(uncoupled_run_dir, cfg, make_move=False)
```

### 1.1 Description and clarification

The following figures compare vector and scalar fields between the outputs of my model, and the figure data from S19. For scalar fields, panel (a) is the data from the model, panel (b) is the data from S19, panel (c) is the different between them (a-b), and panel (d) is the fractional absoloute error error abs((a-b)/b). For the precipitation trend / wind trend plots, panel (a) contains these three fields for the model output, panel (b) contains the output of S19, panel (c) contains the different between them (a-b).

### 1.2 Figure 1d

Text from S19: d–f, Simulations from the ocean model forced by rising CO2 and observed winds (d), observed winds only, with fixed CO2 (e) and rising CO2 with fixed winds (f). The observed SST trend of no warming in the cold tongue amid widespread warming can be reproduced by the ocean model as a combined thermodynamic and dynamic response to CO2 and wind stress change. g, Distribution of 60-year trends in the NINO3.4 SST index (SST averaged over 5° S–5° N and 170° W–120° W) for end dates from 2008–2017 for 88 individual CMIP5 model runs and 35 NCAR LENS runs, together with observational estimates from ECMWF, HadISST, National Centers for Environmental Prediction (NCEP)/NCAR and ERSSTv5 SST analyses. The observed SST trends ending in the current decade are either colder than, or at the very limit of, the range of trends in individual CMIP5 and LENS model runs.

[81]:
```
comp_oc_sst(uncoup_setup, "1d", var="SST", show_plots=True)
```

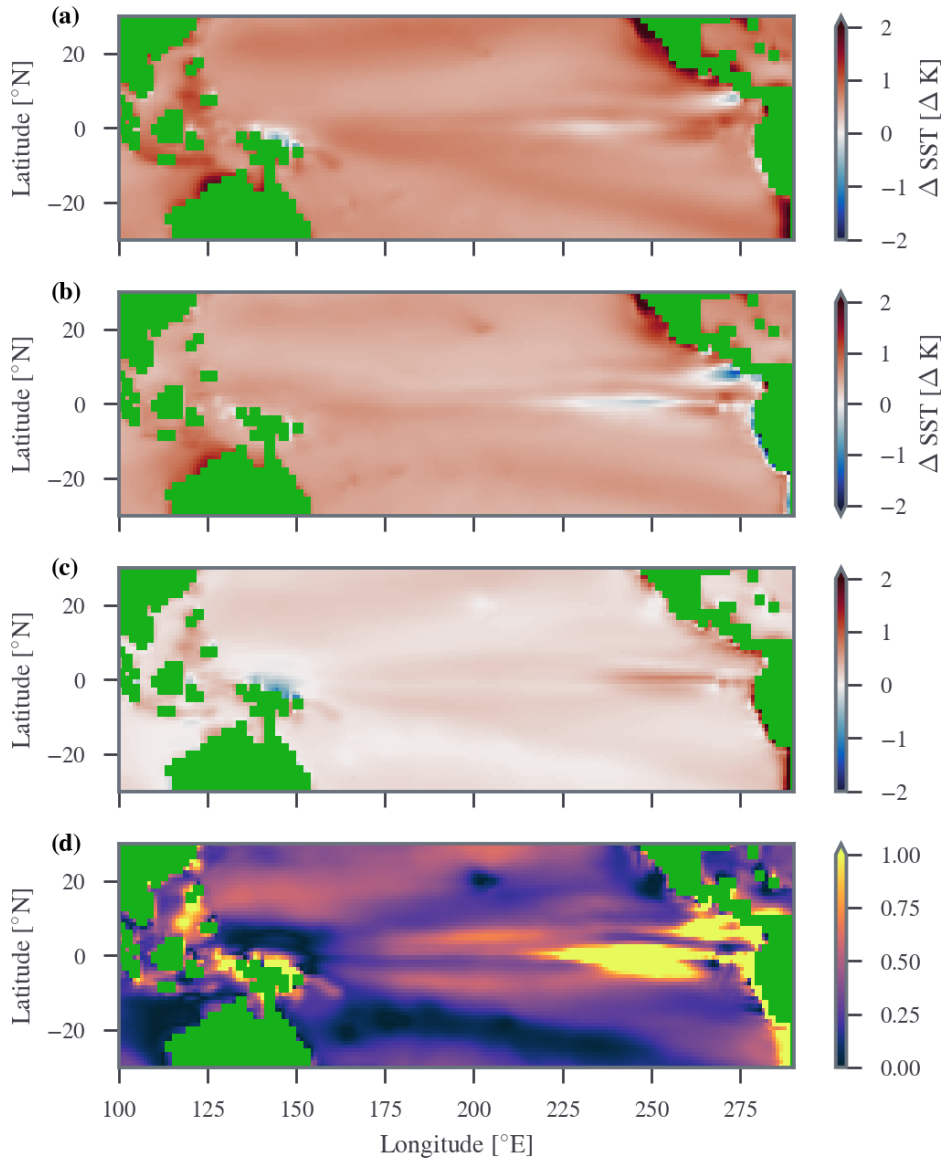


### 1.3 Figure 2d

Text from S19: Trends in surface winds (vectors; the arrow in the bottom right of each panel is a scale bar representing 1 m s−1) and precipitation (colours/contours and numerical labels; see also scale bar), based on ECMWF reanalysis over 1958–2017 simulations by the atmosphere model forced by the observed ECMWF ORAS4 SST trend only (c) and simulations by the atmosphere model forced by trends in ECMWF SST and heating over land (d).

[82]:
```
comp_atm_prwnd(uncoup_setup, "2d", show_plots=True)
```

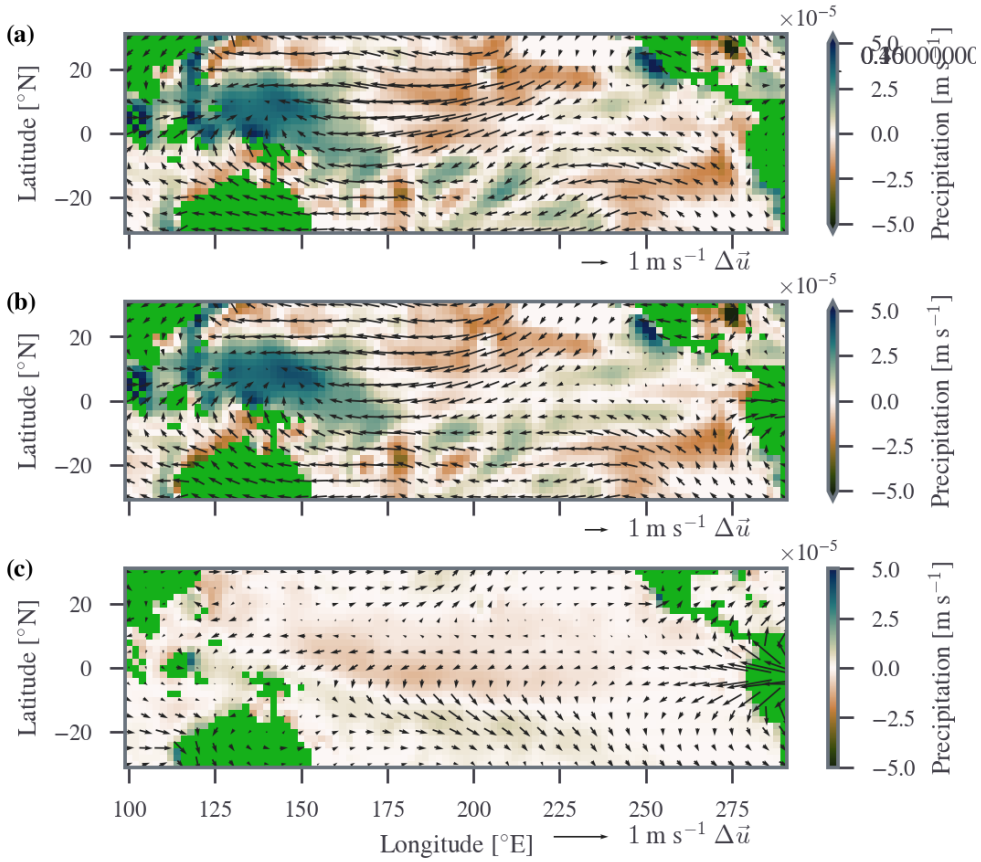


## 1.4 Figure 3

Text from S19: a,b, SST change (a; colours/contours and numerical labels (in K)) and precipitation change (b; colours/contours and numerical labels (in mm d−1) for the model forced only by the CO2 change over 1958–2017 and the precipitation trend over the Amazon. The vectors in b represent change in surface wind vectors (scale bar in m s−1).

[169]:
```
comp_oc_sst(setup_from_name("N_std_coup"), "3", show_plots=True)
```

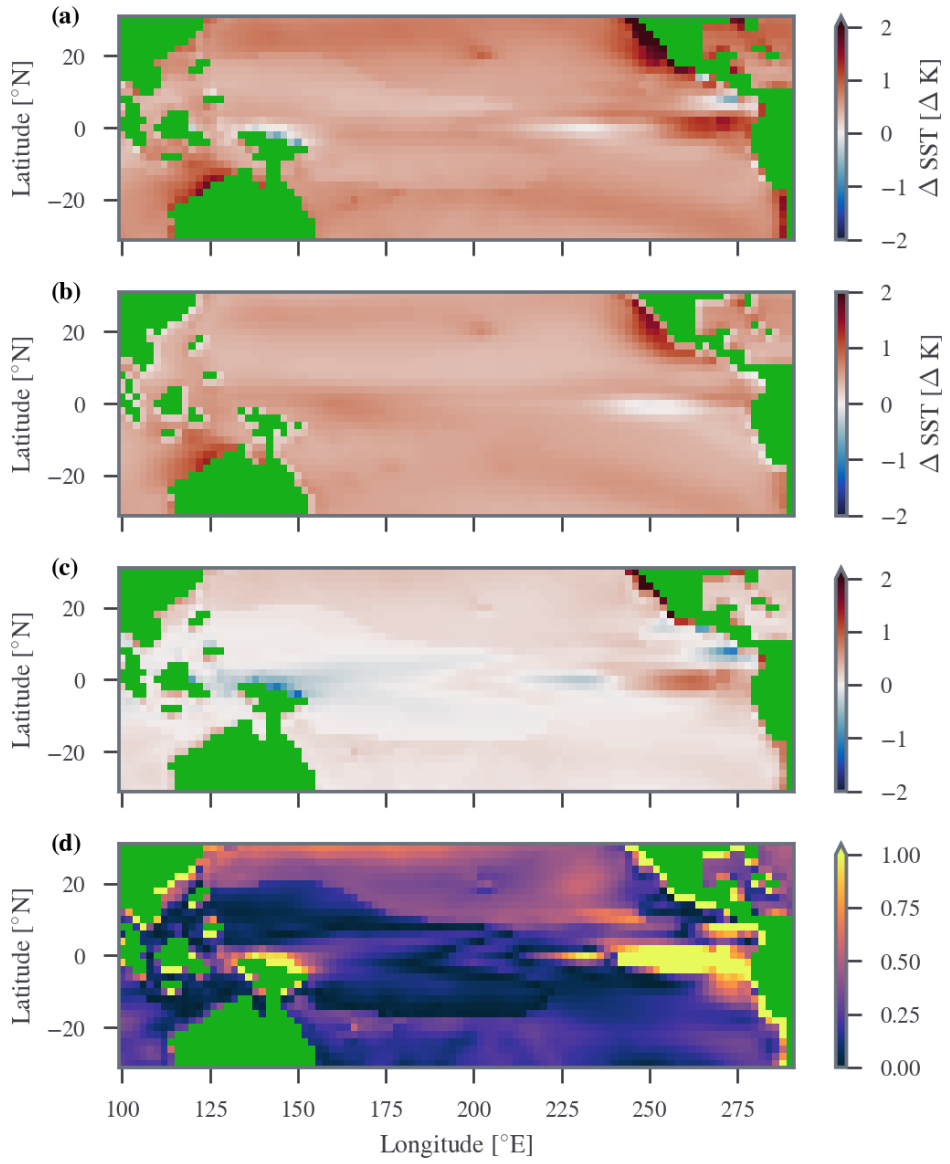


[169]: '/gws/nopw/j04/ai4er/users/sdat2/rep/N_std_coup/plots/fig_3_sst.png'

[174]:
```
comp_oc_sst(setup_from_name("AE_std_coup"), "3", show_plots=True)
```

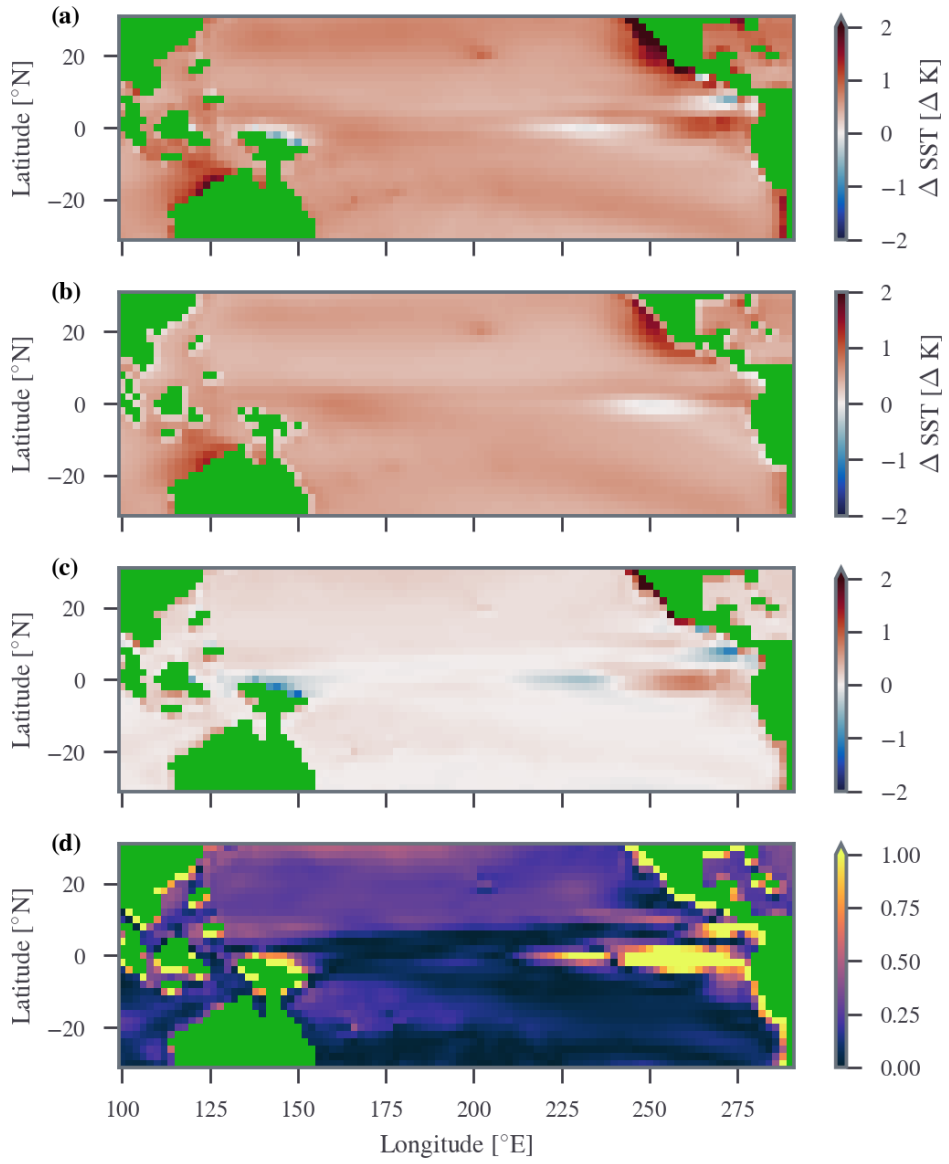


[174]: '/gws/nopw/j04/ai4er/users/sdat2/rep/AE_std_coup/plots/fig_3_sst.png'

[170]:
```
comp_atm_prwnd(setup_from_name("N_std_coup"), "3", show_plots=True)
```

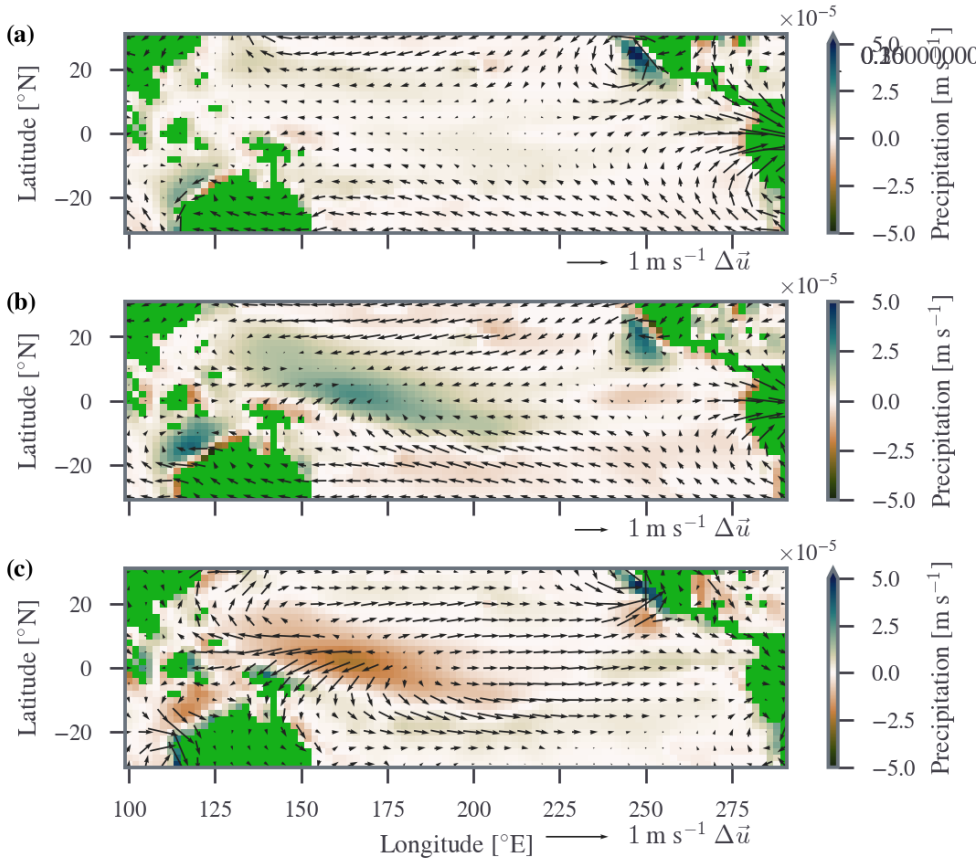


[170]: '/gws/nopw/j04/ai4er/users/sdat2/rep/N_std_coup/plots/fig_3_prwnd.png'

[173]:
```
comp_atm_prwnd(setup_from_name("AE_std_coup"), "3", show_plots=True)
```

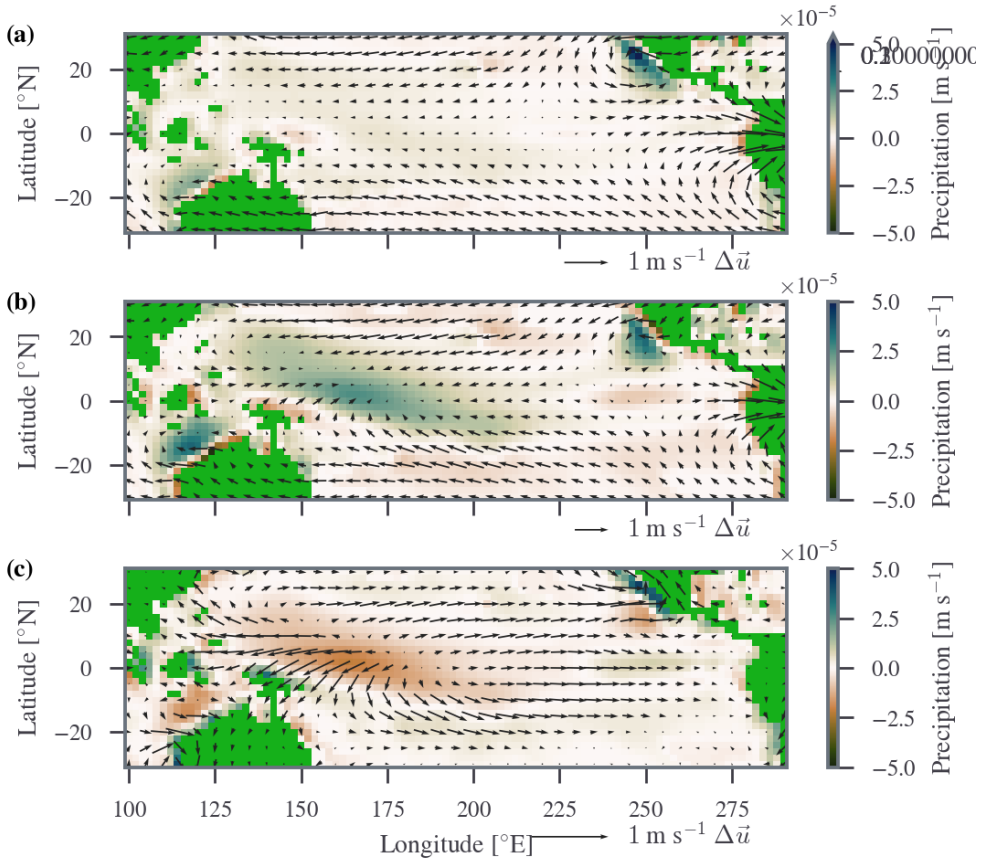


[173]: '/gws/nopw/j04/ai4er/users/sdat2/rep/AE_std_coup/plots/fig_3_prwnd.png'

### 1.5 Figure 4

Text from S19: The ocean model forced by the same winds used to force ORAS4 (b) and the equilibrium state of our coupled atmosphere–ocean model (c). Units for thermocline depth are in m. The coupled model has more wind-forced zonal asymmetry of the equatorial thermocline change than ORAS4, related to differences in equatorial zonal wind stress change. The simulated shoaling in the upwelling region drives the cooling tendency in the cold tongue, and the basin mean component of shoaling is important and driven by off-equatorial trade wind strengthening.

[88]:
```
comp_oc_htherm(uncoup_setup, "4b", show_plots=True)
```

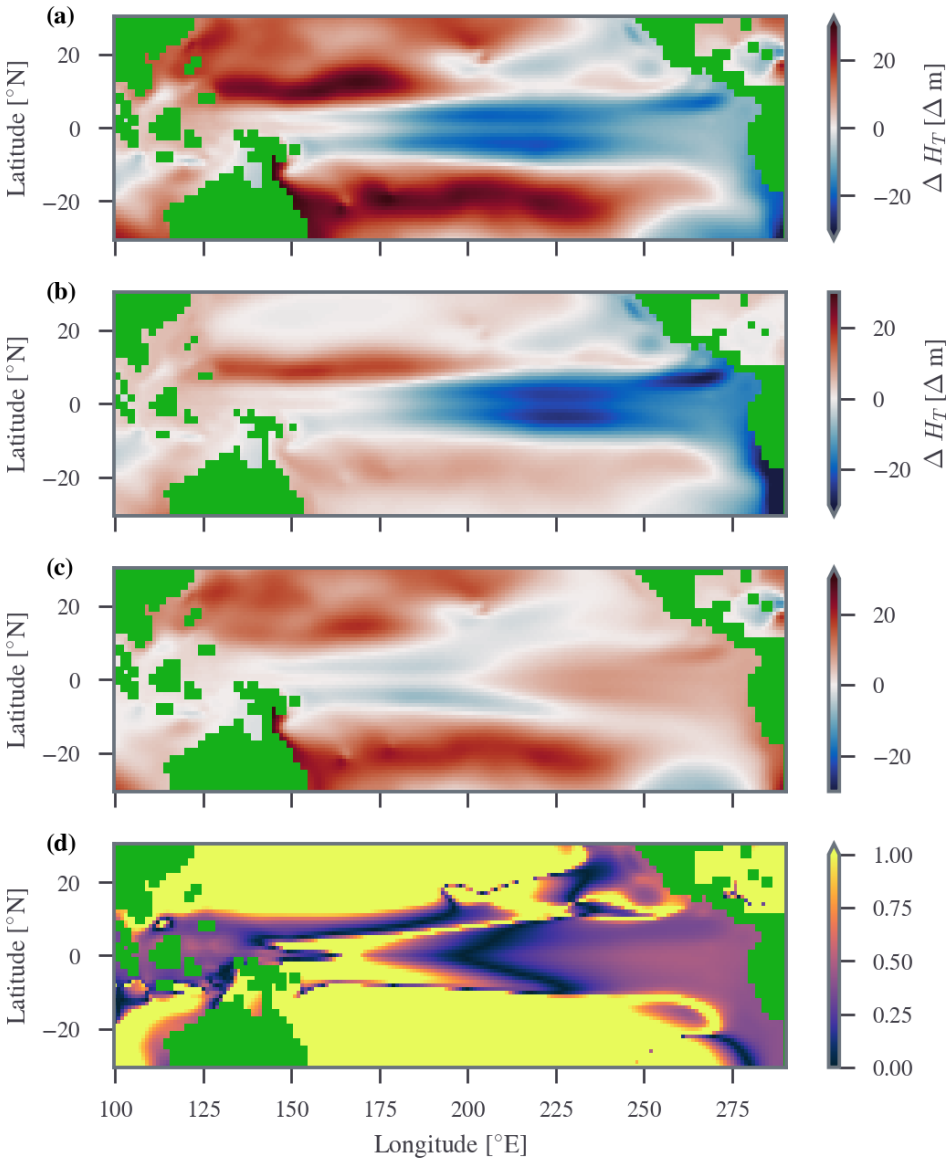


[175]:
```
comp_oc_htherm(setup_from_name("N_std_coup"), "4c", show_plots=True)
```

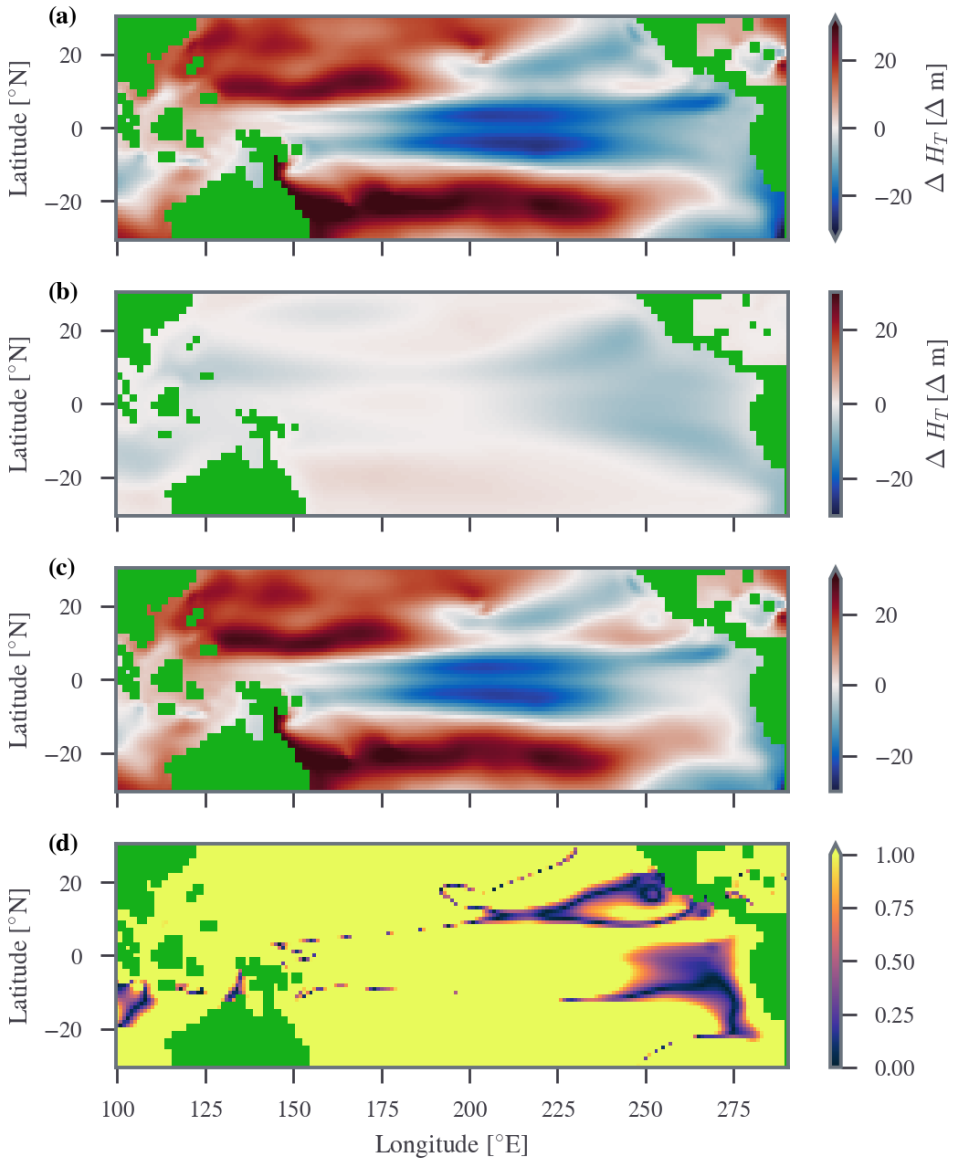


[175]: '/gws/nopw/j04/ai4er/users/sdat2/rep/N_std_coup/plots/fig_4c_htherm.png'

[177]:
```
comp_oc_htherm(setup_from_name("AE_std_coup"), "4c", show_plots=True)
```

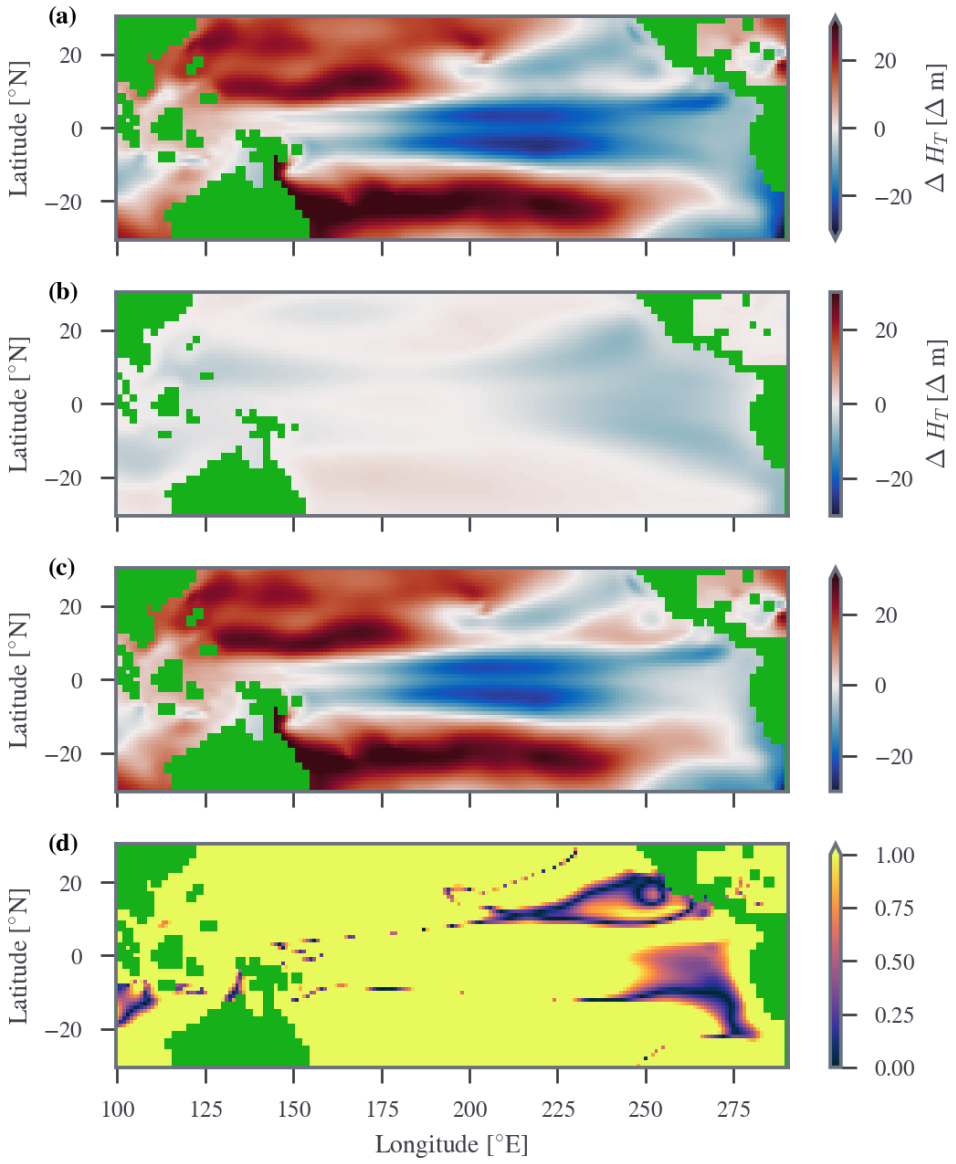


[177]: '/gws/nopw/j04/ai4er/users/sdat2/rep/AE_std_coup/plots/fig_4c_htherm.png'

### 1.6 Figure 5a

a–d, Trends in winds (vectors; scale bar in m s−1) and SST (colours; see scale bar) over 1958–2017 within the coupled model (CM), moving from the observed world to the CMIP5 world. In a, the observed spatially varying relative humidity (%, contours) from ECMWF is imposed in the model instead of a uniform value ('CM-ECMWF world' in e)

[181]:
```
comp_atm_prwnd(setup_from_name("N_ECMWF_coup"), "5a", show_plots=True)
```

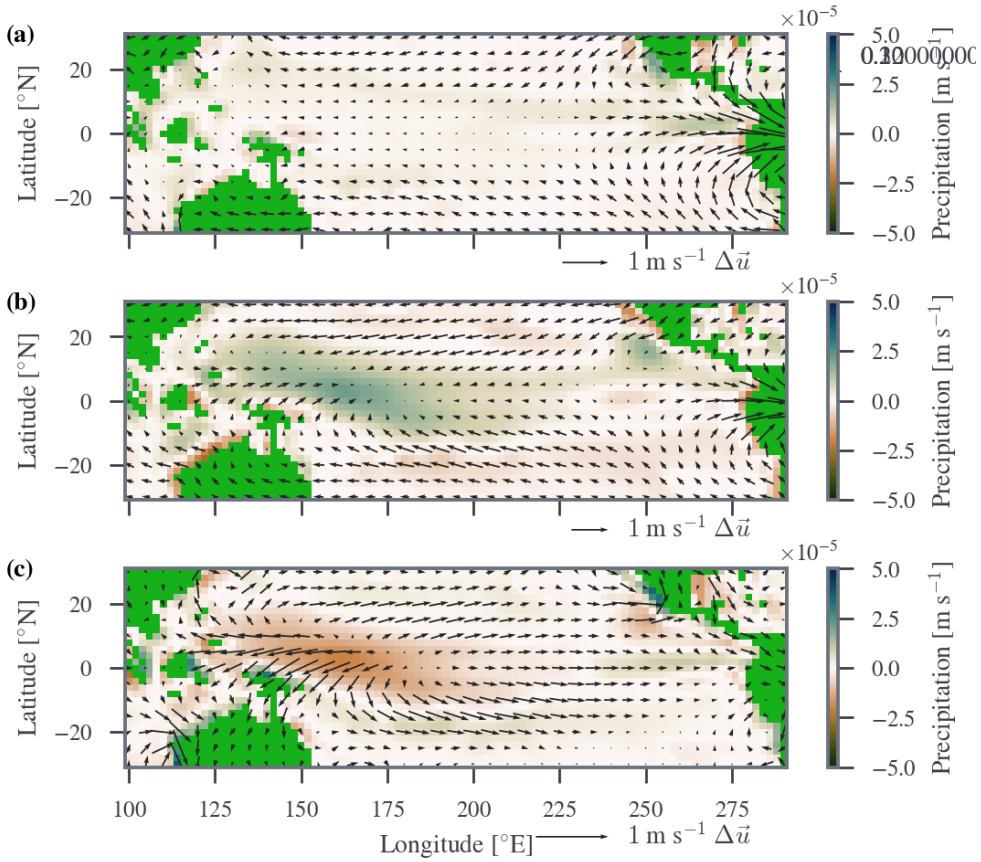


[181]:
```
'/gws/nopw/j04/ai4er/users/sdat2/rep/N_ECMWF_coup/plots/fig_5a_prwnd.png'
```

[182]:
```
comp_atm_prwnd(setup_from_name("AE_ECMWF_coup"), "5a", show_plots=True)
```

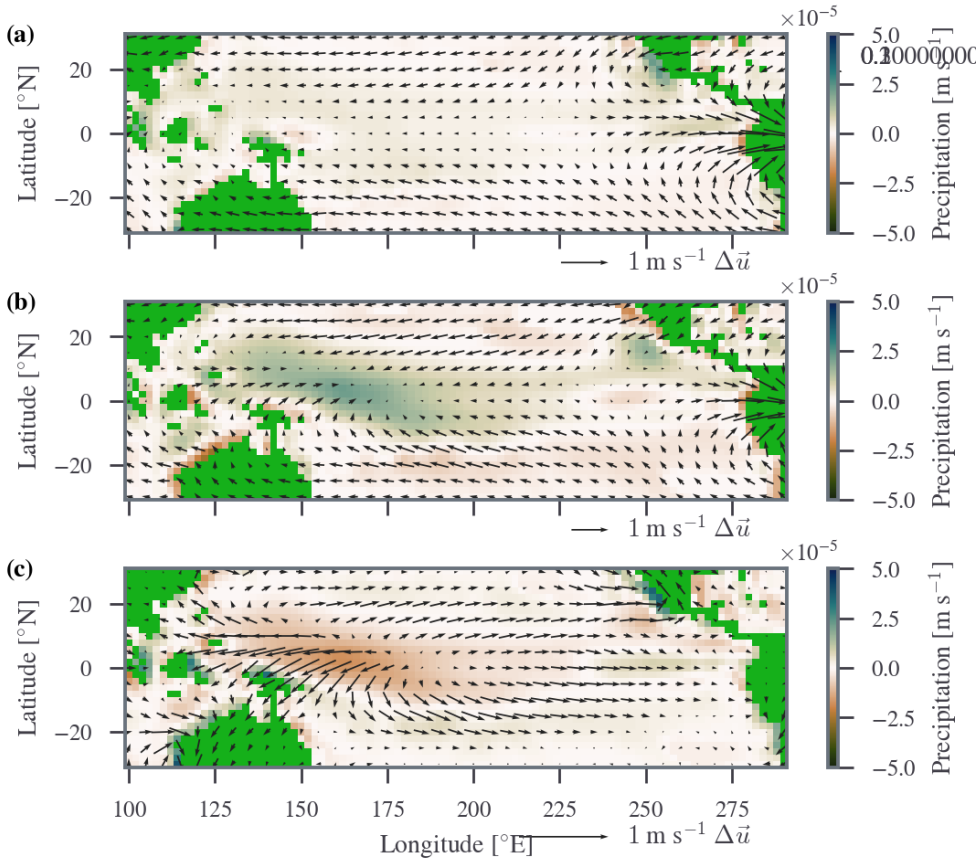


[182]: '/gws/nopw/j04/ai4er/users/sdat2/rep/AE_ECMWF_coup/plots/fig_5a_prwnd.png'

[183]:
```
comp_oc_sst(setup_from_name("N_ECMWF_coup"), "5a", show_plots=True)
```

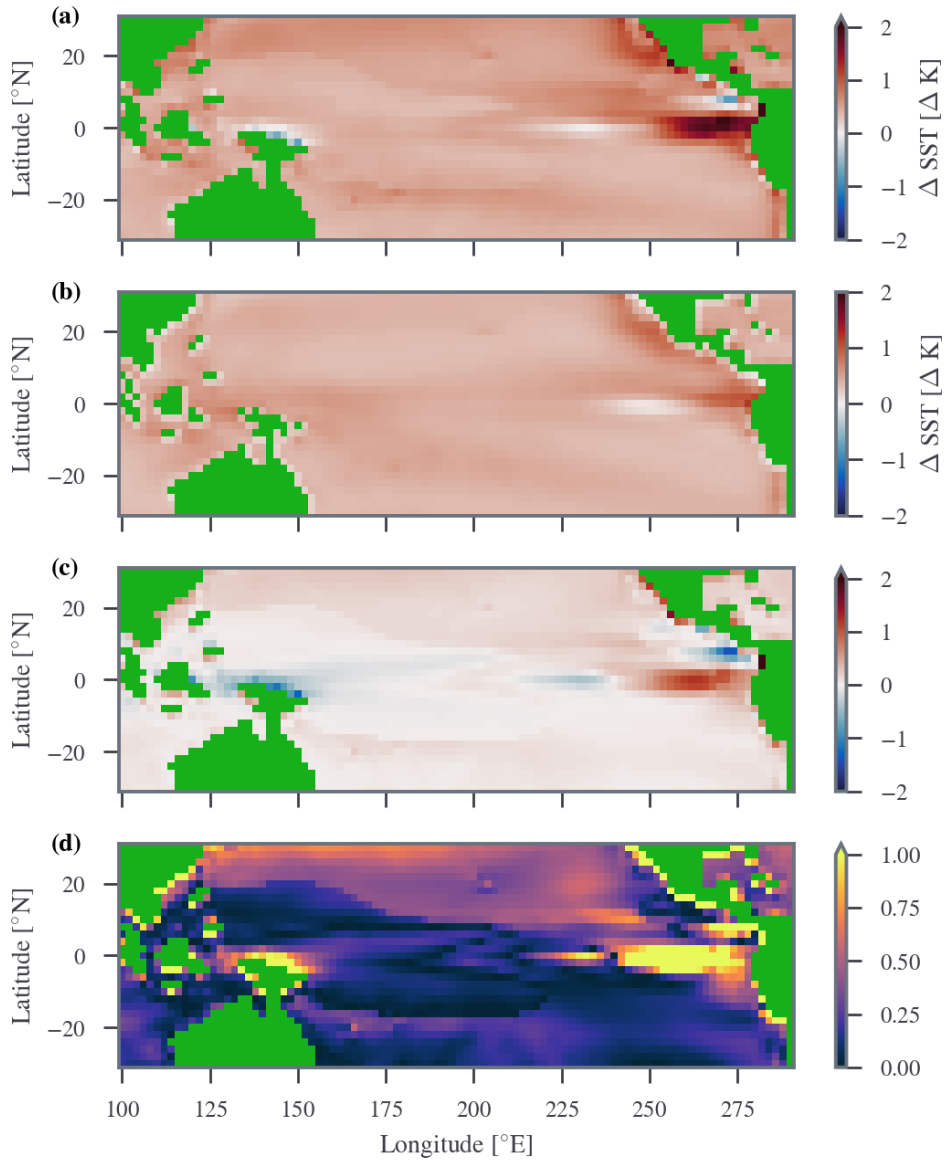


[183]: '/gws/nopw/j04/ai4er/users/sdat2/rep/N_ECMWF_coup/plots/fig_5a_sst.png'

[184]:
```
comp_oc_sst(setup_from_name("AE_ECMWF_coup"), "5a", show_plots=True)
```

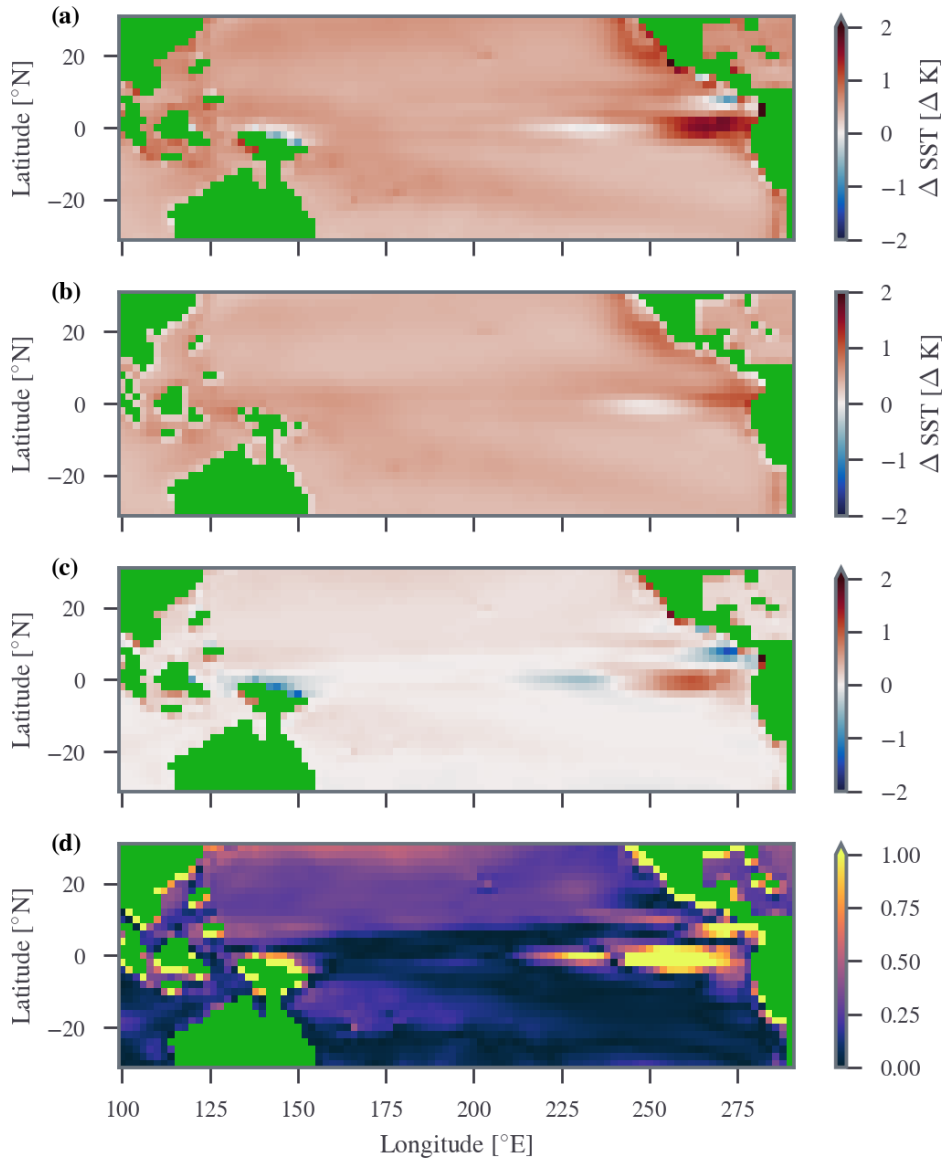


[184]: '/gws/nopw/j04/ai4er/users/sdat2/rep/AE_ECMWF_coup/plots/fig_5a_sst.png'

### 1.7 Figure 5b

[185]:
```
comp_atm_prwnd(setup_from_name("N_C_RH_coup"), "5b", show_plots=True)
```

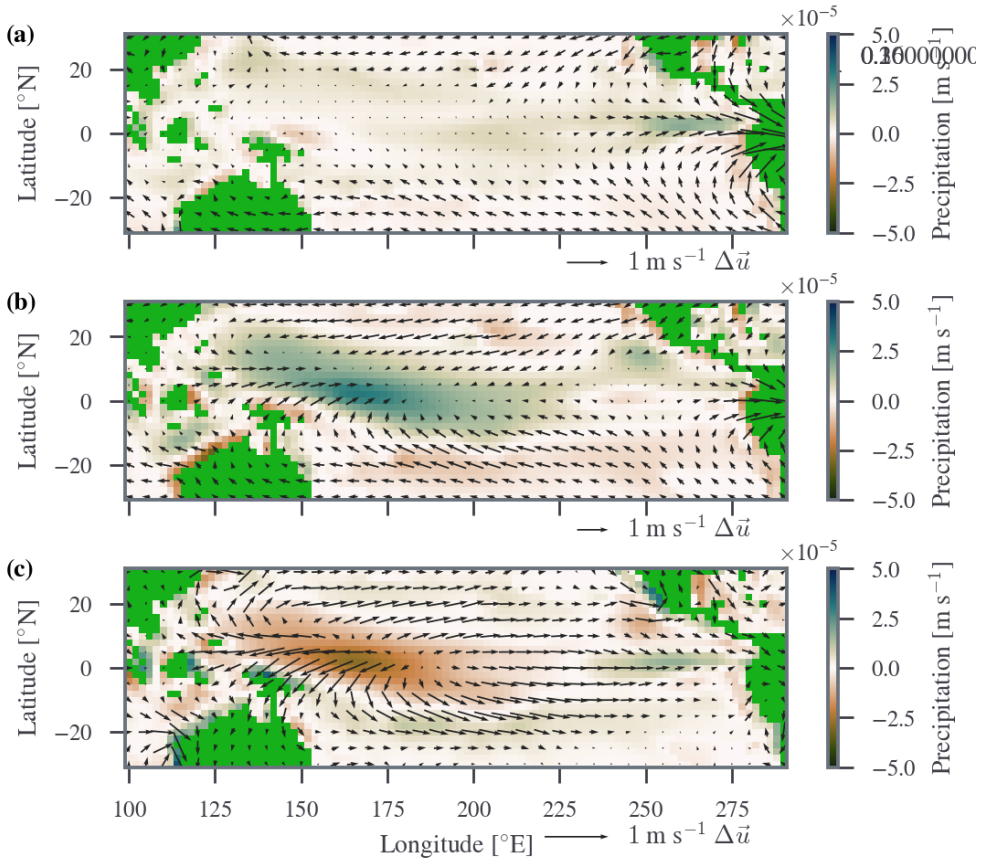


[185]: '/gws/nopw/j04/ai4er/users/sdat2/rep/N_C_RH_coup/plots/fig_5b_prwnd.png'

[186]:
```
comp_atm_prwnd(setup_from_name("AE_C_RH_coup"), "5b", show_plots=True)
```

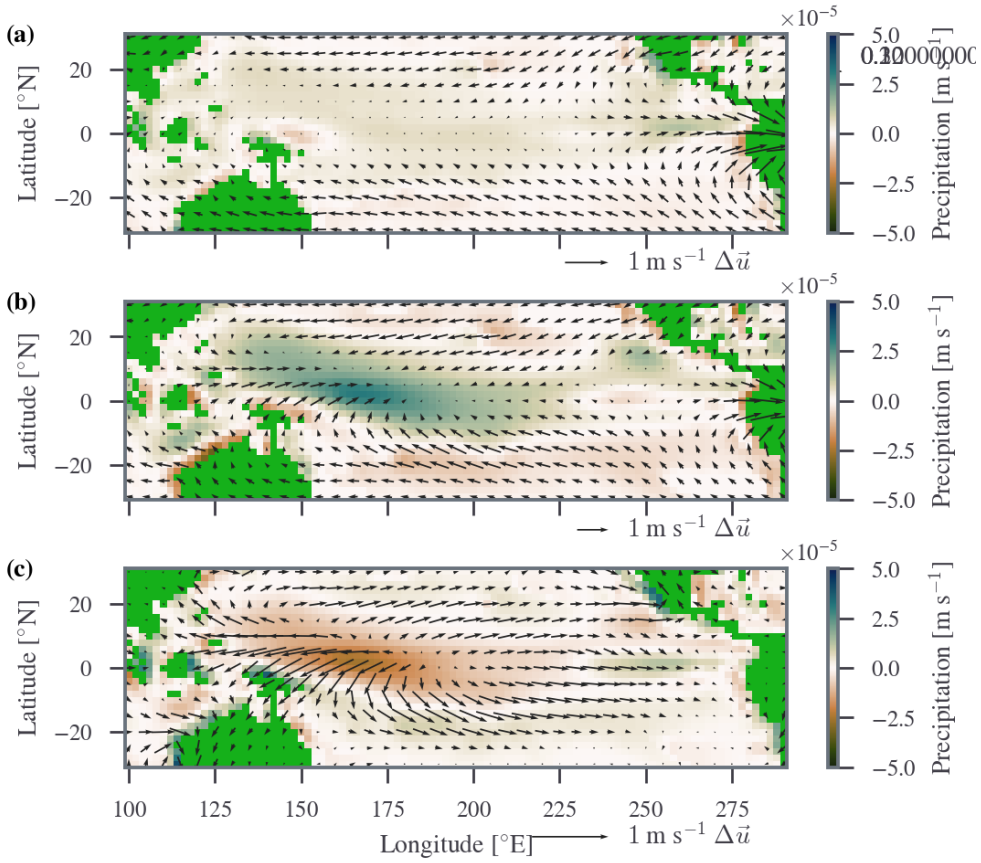


[186]: '/gws/nopw/j04/ai4er/users/sdat2/rep/AE_C_RH_coup/plots/fig_5b_prwnd.png'

[188]:
```
comp_oc_sst(setup_from_name("N_C_RH_coup"), "5b", show_plots=True)
```

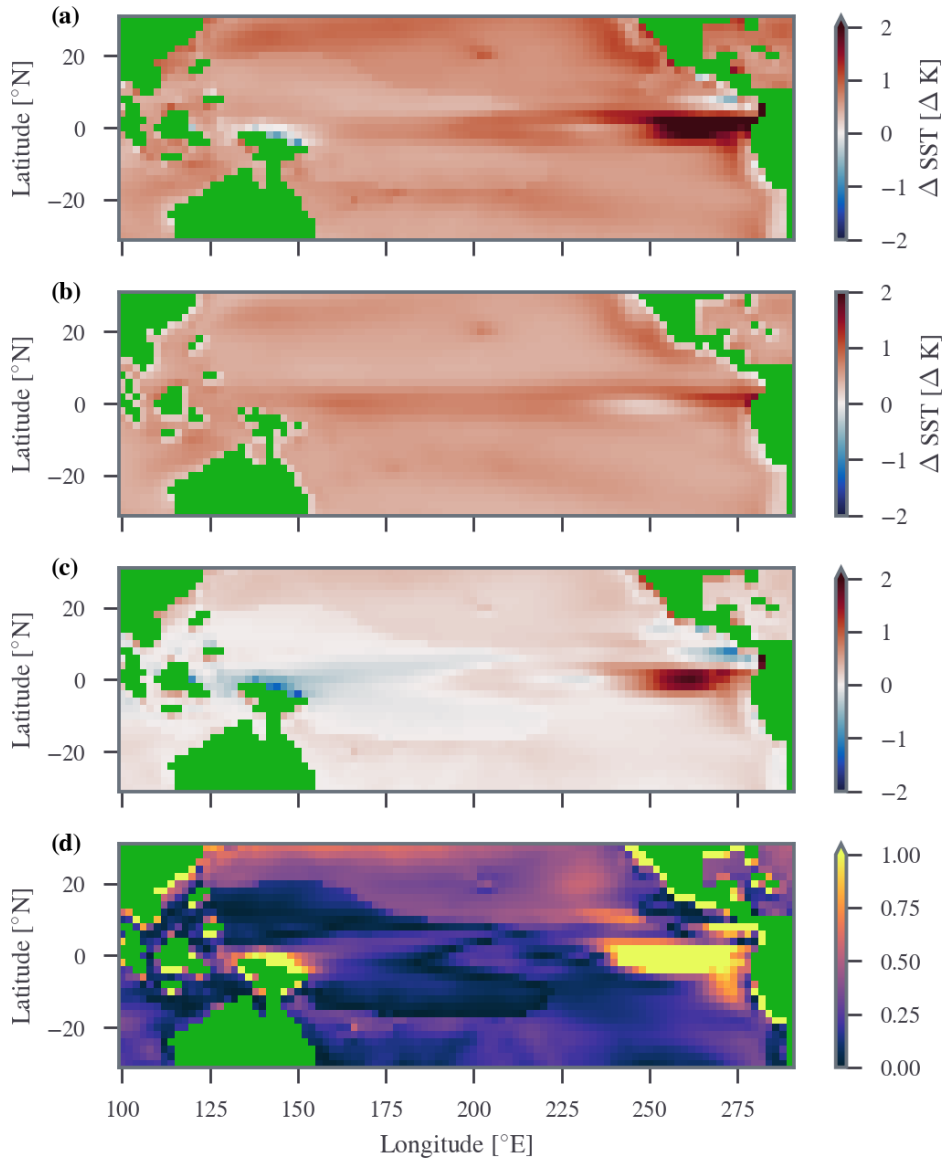


[188]: '/gws/nopw/j04/ai4er/users/sdat2/rep/N_C_RH_coup/plots/fig_5b_sst.png'

[189]:
```
comp_oc_sst(setup_from_name("AE_C_RH_coup"), "5b", show_plots=True)
```

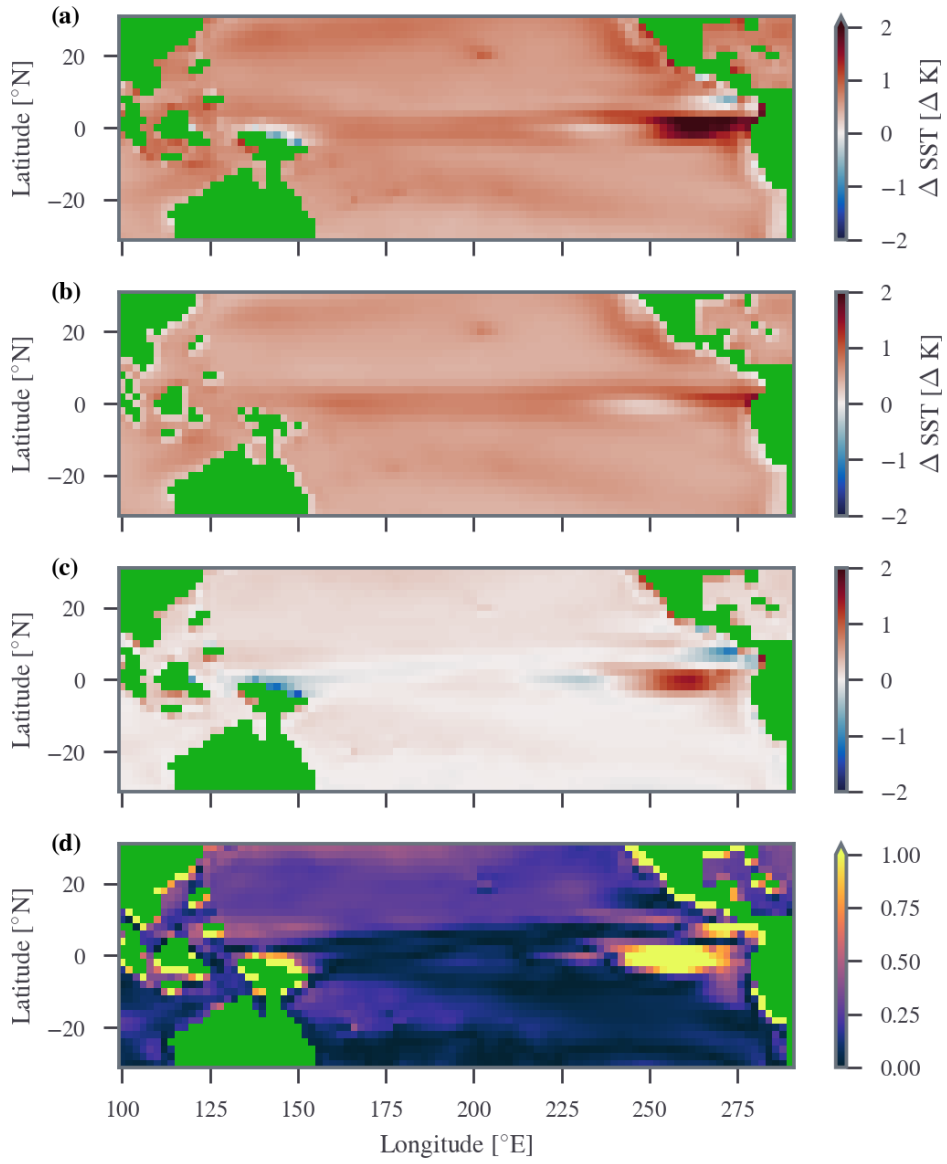


[189]: '/gws/nopw/j04/ai4er/users/sdat2/rep/AE_C_RH_coup/plots/fig_5b_sst.png'

### 1.8 Figure 5c

[192]:
```
comp_atm_prwnd(setup_from_name("N_C_RH_W2_coup"), "5c", show_plots=True)
```

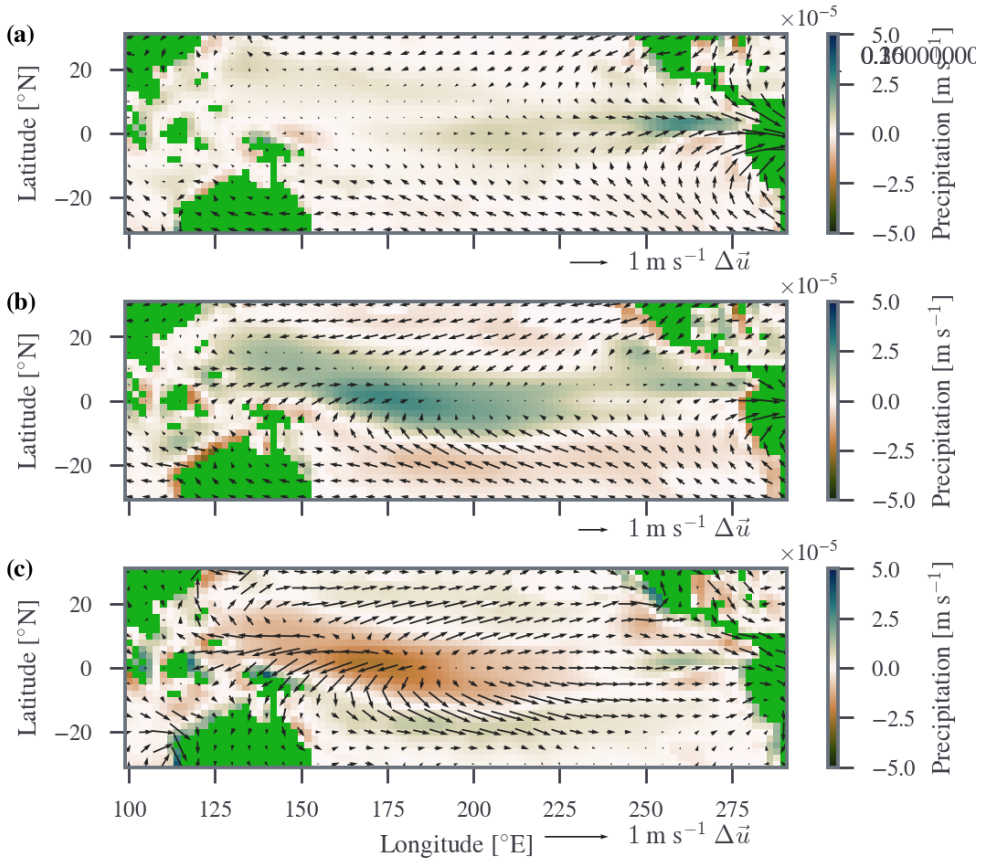


[192]: '/gws/nopw/j04/ai4er/users/sdat2/rep/N_C_RH_W2_coup/plots/fig_5c_prwnd.png'

[193]:
```
comp_atm_prwnd(setup_from_name("AE_C_RH_W_coup"), "5c", show_plots=True)
```

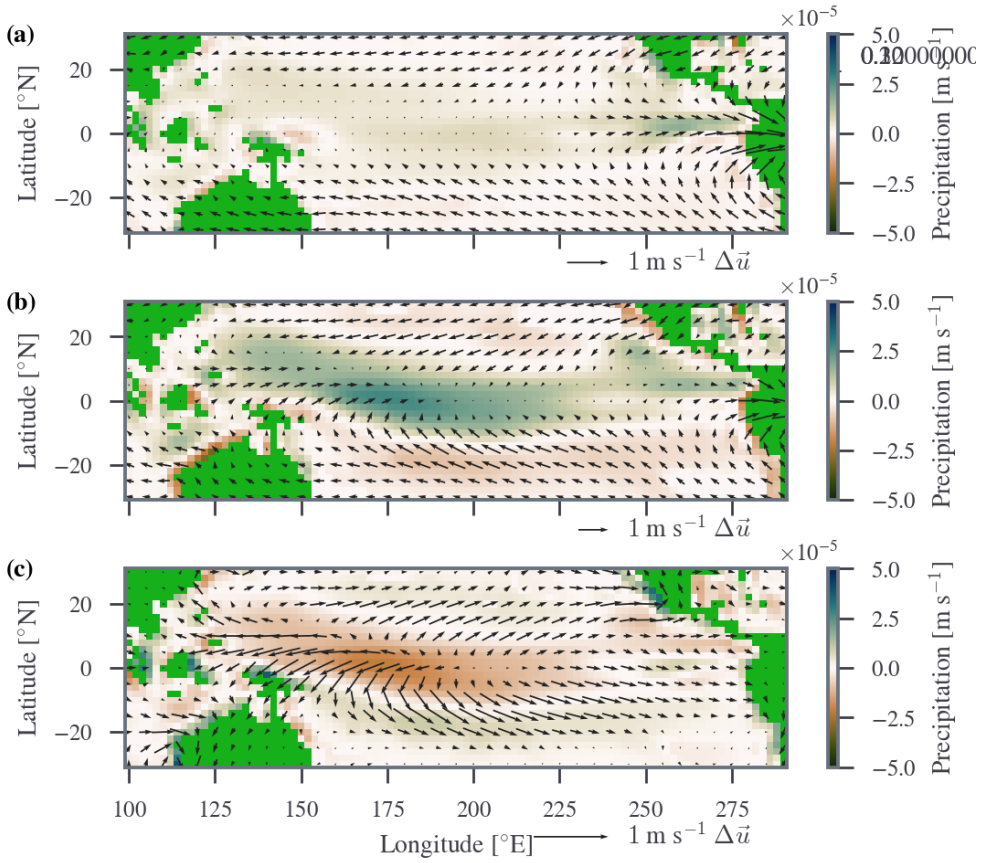


[193]: '/gws/nopw/j04/ai4er/users/sdat2/rep/AE_C_RH_W_coup/plots/fig_5c_prwnd.png'

[191]:
```
comp_oc_sst(setup_from_name("N_C_RH_W2_coup"), "5c", show_plots=True)
```

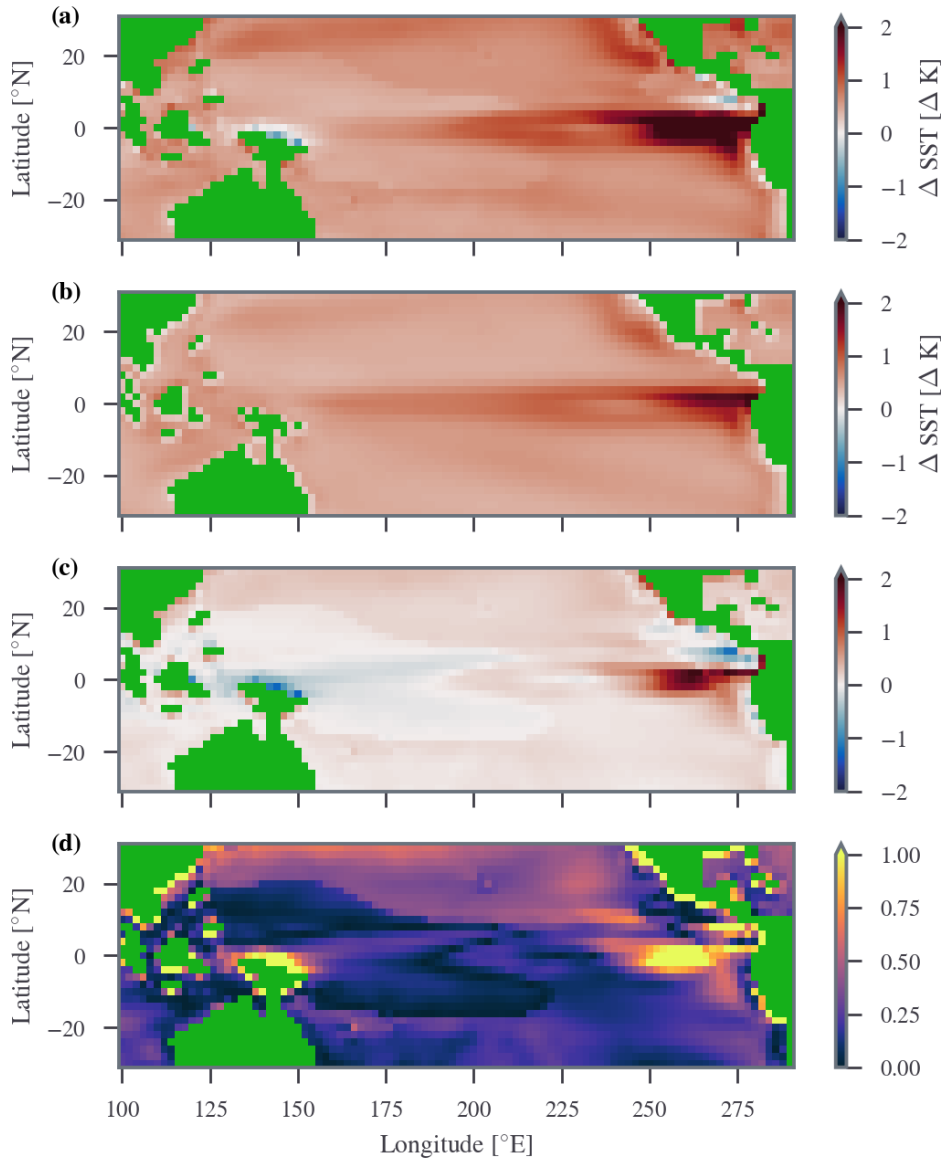


[191]: '/gws/nopw/j04/ai4er/users/sdat2/rep/N_C_RH_W2_coup/plots/fig_5c_sst.png'

[190]:
```
comp_oc_sst(setup_from_name("AE_C_RH_W_coup"), "5c", show_plots=True)
```

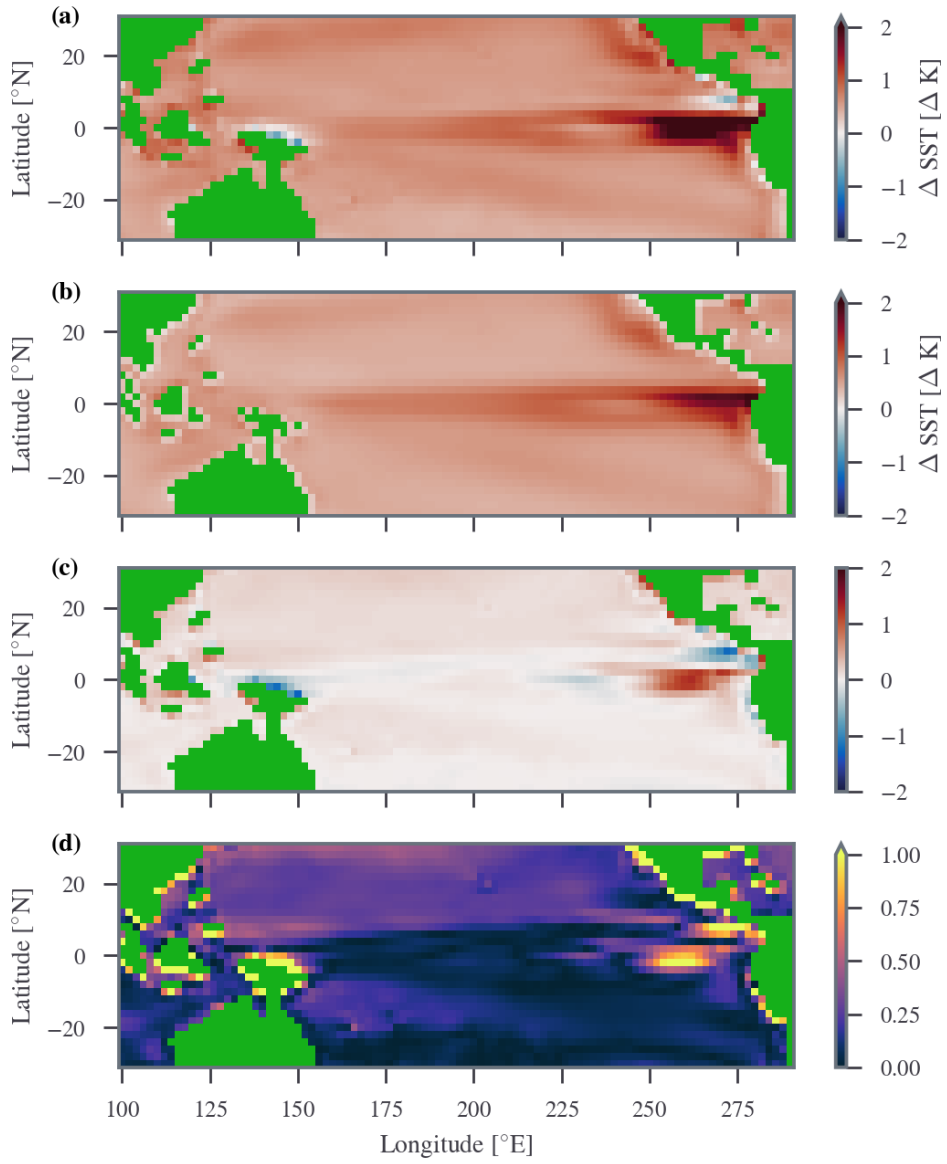


[190]: '/gws/nopw/j04/ai4er/users/sdat2/rep/AE_C_RH_W_coup/plots/fig_5c_sst.png'